

Performance of the ITER ICRH system as expected from TOPICA and ANTITER II modelling

This content has been downloaded from IOPscience. Please scroll down to see the full text.

2010 Nucl. Fusion 50 025026

(<http://iopscience.iop.org/0029-5515/50/2/025026>)

View the [table of contents for this issue](#), or go to the [journal homepage](#) for more

Download details:

IP Address: 165.193.178.118

This content was downloaded on 30/03/2016 at 13:59

Please note that [terms and conditions apply](#).

Performance of the ITER ICRH system as expected from TOPICA and ANTITER II modelling

A. Messiaen¹, R. Koch¹, R.R. Weynants¹, P. Dumortier¹,
F. Louche¹, R. Maggiora² and D. Milanesio²

¹ Laboratory for Plasma Physics-ERM/KMS, EURATOM-Belgian State Association, partner in the Trilateral Euregio Cluster, B-1000 Brussels, Belgium

² Politecnico di Torino, Dipartimento di Elettronica, Torino, Italy

Received 25 September 2009, accepted for publication 13 January 2010

Published 29 January 2010

Online at stacks.iop.org/NF/50/025026

Abstract

The performance on plasma of the antennas of the proposed ITER ICRF system is evaluated by means of the antenna 24×24 impedance matrix provided by the TOPICA code and confirmed and interpreted by the semi-analytical code ANTITER II (summarized in an appendix). From this analysis the following system characteristics can be derived: (1) a roughly constant power capability in the entire 40–55 MHz frequency band with the same maximum voltage in the eight feeding lines is obtained for all the considered heating and current drive phasings on account of the broadbanding effect of service stubs. (2) The power capability of the array significantly depends on the distance of the antenna to the separatrix, the density profile in the scrape-off layer (SOL) and on the strap current toroidal and poloidal phasings. The dependence on phasing is stronger for wider SOL. (3) To exceed a radiated power capability of 20 MW per antenna array in the upper part of the frequency band, with a separatrix–wall distance of 17 cm and a conservative short decay plasma edge density profile, the system voltage stand-off must be 45 kV and well chosen combinations of toroidal and poloidal phasing are needed. (4) On account of the plasma gyrotropy and of poloidal magnetic field, special care must be taken in choosing the optimal toroidal current drive and poloidal phasings.

The ANTITER II analysis shows furthermore that important coaxial and surface mode excitation can only be expected in the monopole toroidal phasing, that strong wave reflection from a steep density profile significantly reduces the coupling even if the separatrix is closer to the antenna and that the part of the edge density profile having a density lower than the cut-off density pertaining to the considered phasing does not significantly contribute to the coupling.

PACS numbers: 28.52.Cx, 52.50.Qt, 52.55.Fa

(Some figures in this article are in colour only in the electronic version)

1. Introduction

The new baseline design of ITER foresees ICRH heating two antennas being installed in equatorial ports, each with a design power capability of 20 MW at a 45 kV limit on the system. The electrical design of these antennas, using a compact array of 24 radiating straps combined in eight triplets by means of passive 4-port junctions (4PJs) [1], was selected in April 2007 [2]. The detailed mechanical design that warrants the rf performances together with the cooling, neutron shielding and mechanical constraints is presently in progress [3]. The coupling performances of the antenna to an external load were optimized for the ITER frequency

band (40–55 MHz) by modelling and measurements on a mock-up loaded by an adjustable water load [4,5]. A view of this mock-up is presented in figure 1, showing only the electric part of the design without the vacuum feedthroughs and further mechanical details given in [3]. In the course of the optimization, which is detailed in [4,5], we first acted on the geometry of the radiating straps surrounded by their strap boxes. The network consisting of the triplet of straps fed in parallel by a 4PJ acts like a single frequency tuned filter, which, while optimizing, is centred in the ITER frequency domain. Inserting an appropriate service stub transformed the single frequency tuned filter into a band-pass filter and avoided the coupling decrease at the edge of the frequency band. The best

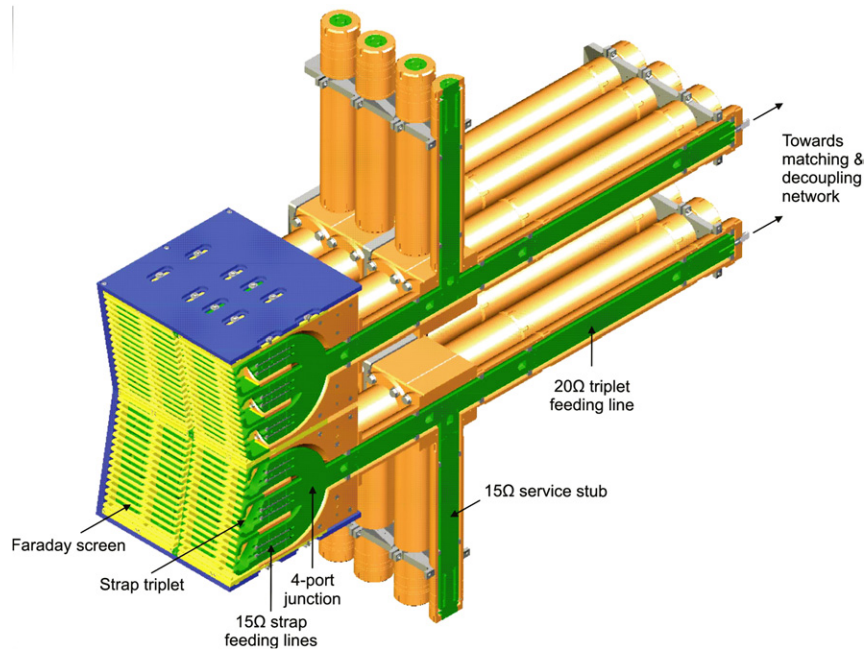


Figure 1. View of the electrical mock-up of the ICRH plug of ITER. The service stubs are not bent as in the detailed mechanical design.

performances were obtained when, for mid-band, the electrical junction point of the 4PJ is at the first voltage anti-node and the service stub insertion point is near the next voltage node. The length of the service stub is around a quarter mid-band wavelength.

The load resilient matching and feeding system have also been selected. Four quadrature hybrids are used for obtaining the requested load resilience for operation in Elmy plasmas. Each hybrid is fed by a power source of at least 5 MW and feeds with the same forward power the top and bottom triplet of the same poloidal column of six straps. A matching solution that strongly counteracts the mutual coupling effects between the strap triplets by means of appropriate decouplers is presently studied [6, 7] aiming at a precise adjustment of the radiating strap current spectrum by the feedback control of the anti-node voltages in the eight feeding lines and this with the power sources preset at the same forward power.

The aim of this paper is to study the expected performances of the design when loaded by plasma. In section 2, we detail the specific ITER ICRH system layout [3, 4] and the formalism for its modelling based on the antenna array impedance matrix provided by the TOPICA code [8, 9] and using edge plasma density profiles provided by ITER. The performance expectation thus obtained is given in section 3. Important differences in plasma coupling, depending on array phasing, are obtained, which call for additional physics understanding. Therefore, in section 4, this physics interpretation is generated by means of the cruder, semi-analytical but fast coupling code ANTITER II (the details of which are given in an appendix). The same code is also used to separate out the possible contribution in the TOPICA coupling of undesirable coaxial or surface modes and to study in detail the sensitivity of the antenna coupling to the plasma profile modifications.

A first summary of the main results has been given in [10] and some results given in [11, 12].

2. Formalism of the modelling of the system performance with plasma loading

2.1. Detailed system layout and rationale

The layout of the complete ICRH system proposed for ITER is shown in figure 2. The antenna proper will be housed in an antenna plug. A decoupler and tuning network will be located outside of this plug and fed from the generators via 3 dB hybrid splitters and transmission lines.

The electrical hardware inside the antenna plug for the present status of design is presented in figure 1. Please note in the first place the complete array of four pairs of triplets covered by the Faraday screen. A poloidal cut of the first poloidal pair of triplets shows how each triplet of straps is fed in parallel by a 4PJ through three sections of length l_{11} , l_{12} , l_{13} of coaxial line (of characteristic impedance $Z_{01} = 15 \Omega$). The present 4PJ design (shown in figure 1) is used for the computation of its 4×4 scattering matrix by MicroWave Studio (MWS) [13]. Each strap has its own strap box and the mean electrical length $\langle l_1 \rangle = (l_{11} + l_{12} + l_{13})/3$ is chosen to have the first voltage anti-node at the electrical junction point at a frequency f_0 near the ITER mid-band. Each triplet is connected to the external matching network by a $Z_{02} = 20 \Omega$ line. At a distance $l_2 \sim \lambda_{\text{mid-band}}/4$ from the junction point a service stub of characteristic impedance $Z_{0SST} = 15 \Omega$ is inserted in parallel. Its length also corresponds to $\sim \lambda_{\text{mid-band}}/4$ [4]. In the detailed mechanical design [3] this service stub is bent and folded for space saving.

As seen in figure 2, eight feeding lines protrude from the antenna plug, leading through eight line stretchers (allowing to preset for any frequency in the ITER band a voltage anti-node at preset locations A, B, ..., H at a distance l_3 from the service stubs) to a decoupling and matching circuit. This system is then fed by four power sources through quadrature 3 dB hybrid junctions that provide the needed load resilience

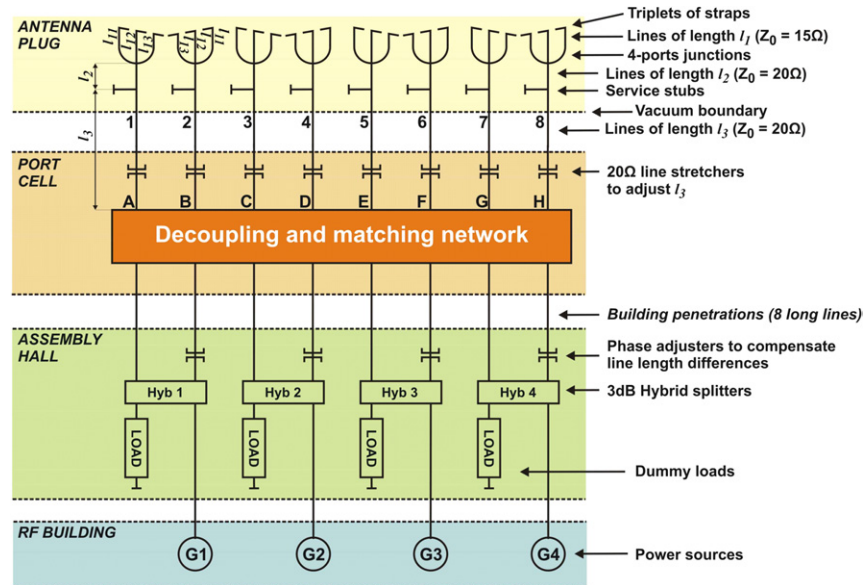


Figure 2. Schematic layout of the ICRH antenna plug with its feeding through hybrid power splitters, matching and decoupler network by four power sources.

for operation in an Elmy plasma by dumping the reflected power in the dummy loads.

The analysis of the global circuit from data and tests on a mock-up [6] brought forward the following important properties: (i) the current spectrum of the triplets of straps can be accurately controlled in phase and amplitude by the specific distribution of the voltages $V_{\max 3}$ over the locations A, B, ..., H in the feeding lines; (ii) the amplitude of these voltages $|V_{\max 3}|$ (normally set to equal values) can be feedback controlled by the decoupler circuit, with equal forward power P_{G+} of the four power sources; (iii) the toroidal phasing between the four poloidal pairs of triplets can be preset by the phase difference between the power sources because the phase difference introduced by each tuner is the same when all $|V_{\max 3}|$ are equal and all P_{G+} are equal; (iv) the poloidal phasing between the triplets of each poloidal pair is imposed by the hybrid at $\pm\pi/2$ depending on their connection to the hybrid. Because of these properties, the response of the global ICRH system can be inferred from the imposition of an appropriate $V_{\max 3}$ distribution over the points A to H.

This is particularly useful to study the response of the antenna plug to the different toroidal phasings for heating (case 1: $0\pi 0\pi$, case 2: $0 0 \pi\pi$, case 3: $0\pi\pi 0$) and current drive (case 4: $0\pi/2\pi 3\pi/2$, case 5: $0-\pi/2-\pi-3\pi/2$). For case 1, for example, the appropriate distribution is $V_{\max 3} = |V_{\max 3}| \cdot \Xi$, where Ξ is the vector $[1; \exp(i\Delta\Phi_{\text{pol}}); -1; -\exp(i\Delta\Phi_{\text{pol}}); 1; \exp(i\Delta\Phi_{\text{pol}}); -1; -\exp(i\Delta\Phi_{\text{pol}})]$ defining the phasing of the eight triplets, going from 1 to 8 (see triplet numbering in figure 3). $|V_{\max 3}|$ is the chosen common maximum voltage amplitude in the feeding lines and $\Delta\Phi_{\text{pol}} = \pm 90^\circ$ is the phase difference between the triplets of each poloidal row imposed by the hybrid junctions.

All details concerning the matching and the effect of the decouplers on the active power distribution among the eight plug input lines to obtain the same $|V_{\max 3}|$ values and the resulting strap current distribution are described in section 5 of [6].

2.2. Modelling the performance with plasma by TOPICA

In all the simulations presented, it is assumed that the mid-plane of the antenna straps (of 3 cm thickness) is located 6 cm inside the ITER wall aperture housing the antenna plug: the Faraday screen has its front recessed 1 cm behind the wall, a thickness of 2 cm and there is a gap of 1.5 cm between its rear part and the front of the straps. The triplet and strap numbering is shown in figure 3 in relation to the magnetic field and plasma current directions of the ITER baseline design. The TOPICA code [9] provides, for the antenna design geometry, the 24 ports scattering matrix S_{24} of the plasma loaded straps array at the connection to their respective 15Ω feeding lines (at output of the strap box). From the TOPICA matrices at 40, 46.5 and 53 MHz a spline fit computes the S_{24} matrices for the entire ITER frequency domain. From this S_{24} matrix and the 4PJ matrix S_4 the eight ports scattering matrix at the 20Ω feeding lines output is computed for the positions labelled 1–8 in figure 4. The differences in length between l_{11} , l_{12} and l_{13} are taken into account to connect the S_{24} to the eight S_4 scattering matrices by shifting the reference planes of S_{24} along the 15Ω lines by the relation $S'_{24} = M S_{24} M$. In this relation M is a 24×24 diagonal matrix of elements $\exp(-i\beta l_n)$, $\beta = \omega/c$ is the vacuum propagation constant and the 24 lengths l_n ($n = 1$ to 24) are given by the l_{1i} with $i = 1$ to 3 for the eight identical triplets connected to their 4PJ. As said earlier, the mean electrical length $\langle l_1 \rangle = (l_{11} + l_{12} + l_{13})/3$ is chosen to have the first voltage anti-node at the electrical junction point at f_0 . Generalized scattering matrices have to be used because the characteristic impedance is not the same at each port. The service stubs are accounted for by adding their admittance matrix to the admittance matrix of the eight 20Ω feeding lines at their insertion position. Then the scattering (S), impedance (Z) and admittance (Y) matrices can be computed at any location of the in-plug circuit shown in figure 4 up to the points A to H. If in these points a $V_{\max 3}$ voltage distribution is applied, the resulting power, voltage and current distribution can be obtained in all the locations of the circuit.

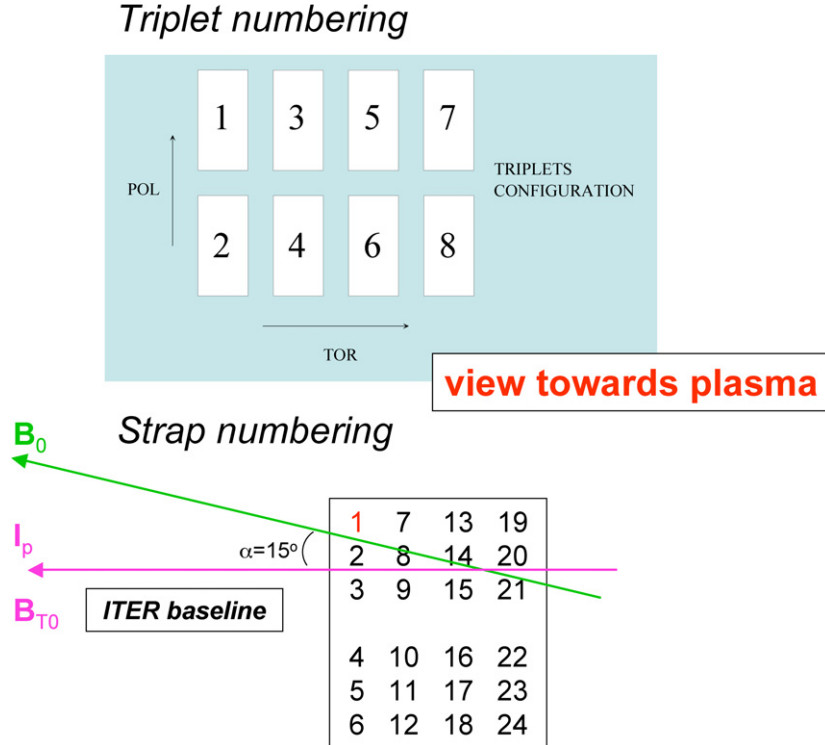


Figure 3. Triplet and strap numbering with the baseline direction of steady magnetic field B_0 and the plasma current I_p in ITER (also used for ANTITER II modelling). Strap 1 of triplet 1 is taken as phase reference.

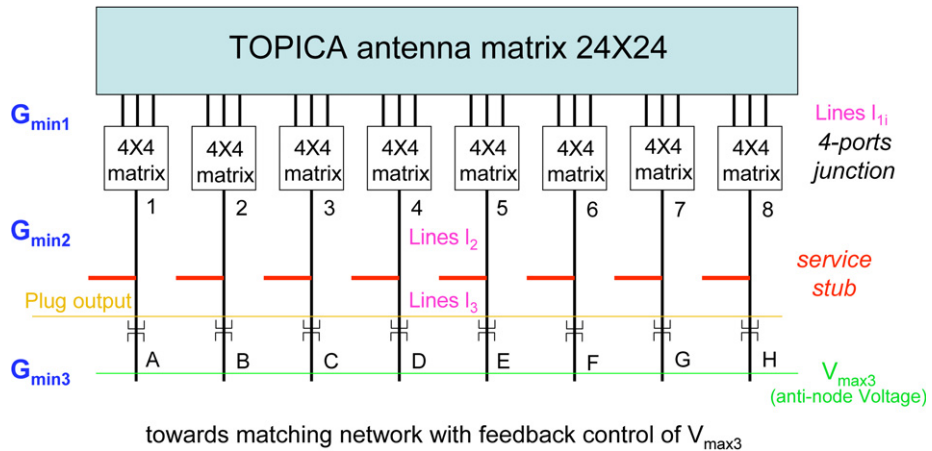


Figure 4. Layout of the modelling of the ITER ICRH antenna plug.

Of particular interest are the line conductances (labelled $G_{\min 3}$, as they correspond to the maximum line voltage) in the points A to H since the total active power P_{tot} coupled to the plasma for a chosen voltage value $|V_{\max 3}|$ in these points can be readily obtained using $G_{\min 3} = 2P_{\text{tot}}/(8|V_{\max 3}|^2)$. The conductivity $G_{\min 3}$ will therefore be used later on to express the coupling capability of the antenna plug for a given value of $|V_{\max 3}|$. We also define in the same way an effective mean minimum conductance $G_{\min 2} = 2P_{\text{tot}}/(8\langle|V_{\max 2}|\rangle^2)$ and $G_{\min 1} = 2P_{\text{tot}}/(24\langle|V_{\max 1}|\rangle^2)$ for the line sections l_1 and l_2 (see figure 2). $\langle|V_{\max}| \rangle = \frac{1}{8} \sum_{l=1}^8 (|V_{l+}| + |V_{l-}|)$ is the average of the sum of the amplitudes of the forward and backward voltages $|V_+|$ and $|V_-|$, and G_{\min} is linked to the mean voltage

standing wave ratio $\langle S \rangle$ in the corresponding line sections by $G_{\min} = 1/(\langle S \rangle Z_0)$.

Please note the strap and triplet numbering convention shown in figure 3. The strap and triplet labelled 1 are taken as phase reference for the assumed toroidal and poloidal phasings. In the following, we will consider three cases of toroidal phasing aimed at heating and two cases for current drive, as already defined at the end of the previous section. A poloidal phasing of $-\pi/2$ is chosen because it has the best coupling for the feeding by quadrature hybrids, as will be discussed later. The sign of poloidal phasing quoted is that of the currents flowing in the straps and therefore seen by the plasma. There is a phase reversal with respect to their feeder phasing because

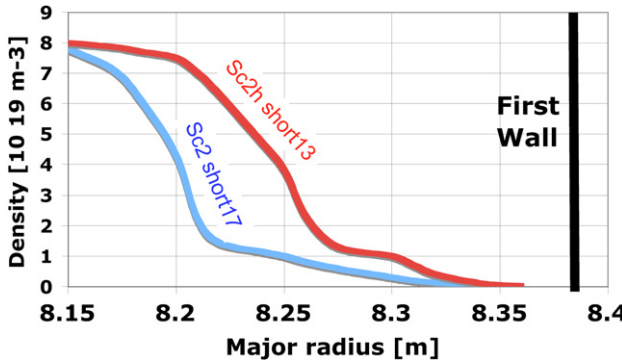


Figure 5. Density profiles ‘Sc2 short 17’(taken as reference) and ‘Sc2h short 13’ used for the coupling computation.

the straps of top and bottom triplets are fed, respectively, from the top and from the bottom.

The plasma load in TOPICA is characterized by two density profiles with short density decay, provided by the ITER organization [14] (based on modelling described in [15]), shown in figure 5, and labelled ‘Sc2 short 17’ and ‘Sc2h short 13’. The distance separatrix–wall is 17 cm and 13 cm, respectively, and the distance from wall to the front plane of the radiating straps is 4.5 cm in each case. While profile Sc2 short 17 is less optimistic than its counterpart, it is considered to be a realistic working hypothesis.

3. Performance expectation from TOPICA for the different phasing conditions versus frequency

3.1. Evolution of G_{\min} versus frequency

Figure 6 displays the response curve of $G_{\min 3}$ in the frequency range from 35 to 60 MHz for the five toroidal phasing cases considered using profile Sc2 short 17. The corresponding (dashed) curves of $G_{\min 2}$ for the phasing cases 1 and 4 give the response curve of the antenna plug in the absence of service stubs. Figure 7 displays the same data for profile Sc2h short13 for comparison.

From these results we can conclude:

- (i) The broadbanding effect of the service stub studied for a single triplet [4] is maintained for the whole array and this for any phasing. Without service stub the plug acts as a filter centred on f_0 . The addition of the service stub transforms this filter to a band-pass one with a quasi-constant value of $G_{\min 3}$ in the ITER frequency band (40–55 MHz). When the plasma comes closer the same uniform response is maintained at a higher value (see figure 7).
- (ii) The present design of the 4PJ is close to the optimum. For the frequency $f = f_0$ we must have $G_{\min 3} = G_{\min 2} = 3G_{\min 1}$ for an ideal 4PJ, i.e. corresponding to three ideal lines of same length merging in one point [16]. Our computed value of $G_{\min 3}(f_0) = G_{\min 2}(f_0)$ is only $\sim 10\%$ below $3G_{\min 1}(f_0)$ as shown for case 2 in figures 6 and 7.
- (iii) There is a large influence of the phasing on the coupling capability as expressed by $G_{\min 3}$. The best coupling occurs for the heating case 2 ($0\ 0\ \pi\ \pi$) and the current drive case 4 ($0\ \pi/2\ \pi\ 3\pi/2$). An increase in the relative plasma–antenna distance has two effects. Firstly, as expected, the

coupling capability decreases and secondly the spread of $G_{\min 3}$ increases. Indeed, the ratio of $G_{\min 3}$ between cases 2 and 1 at 46 MHz is 1.75 and 1.37 for profiles Sc2 short 17 and Sc2 short 13, respectively.

3.2. Voltage and current on the antenna straps

The VSWR being large in the lines l_1 and l_2 , the voltage and current distribution in these lines is strongly correlated with the one of $V_{\max 3}$. Therefore for equal values of $|V_{\max 3}|$ the 24 strap feeding current amplitudes are almost equal with a relative standard deviation of less than 3% for the different phasing cases as shown in figure 8(a). The mean amplitude of these currents at a given frequency remains approximately the same for all phasing conditions as shown in figure 8(b). The phasing of the triplets corresponds accurately to the one of the $V_{\max 3}$, as shown in figure 9 for a current drive case (see also [6]). The strap input voltages are also close to each other for a given frequency and do not change much when the phasing or the plasma profile is modified. This is illustrated in figures 10(a) and (b). This is consistent with the fact that the strap box effective averaged input impedance $\langle Z_{\text{Aeff}} \rangle = \langle R_{\text{Aeff}} \rangle + i \langle X_{\text{Aeff}} \rangle = \sum_i Z_{\text{Aeff},i}/24$ (with $Z_{\text{Aeff},i} = 2P_{\text{A},i}/|I_{\text{A}}|^2$ and $P_{\text{A},i} = V_{\text{A},i}I_{\text{A},i}^*/2$, $i = 1$ to 24) is characterized by $\langle R_{\text{Aeff}} \rangle^2 \ll \langle X_{\text{Aeff}} \rangle^2$ and that $\langle X_{\text{Aeff}} \rangle$, for a given frequency, is only slightly dependent on the phasing and the plasma profile. In contrast $\langle R_{\text{Aeff}} \rangle$ is very sensitive to these conditions. This is shown in figure 11.

3.3. Voltage overshoot between the 4PJ and the service stub

At the frequency $f = f_0$ the 4PJ is at voltage anti-node $V_{\max 2}$ and the service stub at the next voltage node. The voltage amplitude between these locations therefore remains lower than $V_{\max 2}$ and, as the service stub is at a quarter wavelength for $f = f_0$, we have $V_{\max 3} = V_{\max 2}$. For $f < f_0$ the voltage anti-node occurs between the 4PJ and the service stub [4] leading to a voltage overshoot of up to 15% at 40 MHz as shown in figure 10(b).

3.4. Power capability versus toroidal and poloidal phasing

The radiated power capability $P_{\text{rad}} = 8(G_{\min 3}|V_{\max 3}|^2/2)$ corresponding to $|V_{\max 3}| = 45$ kV and the plasma edge profile Sc2 short17 was already shown, for the different toroidal phasing cases considered, in figure 6 (left scale) if the voltage overshoot is allowed. In figure 12(a) the performance is given if the maximum voltage is limited to 45 kV everywhere. In the latter case a power capability exceeding 20 MW per antenna array is only obtained for the heating case 2 and the current drive case 4 for frequency between 42.5 and 57.5 MHz. The power capability is, however, significantly larger for profile Sc2h short13 (see left scale of figure 7).

The poloidal phasing $\Delta\Phi_{\text{pol}}$ also has a big influence on the power capability. Figure 13 illustrates this for a heating and a current drive case: the phasing $\Delta\Phi_{\text{pol}} = \pm 90^\circ$ imposed by the quadrature hybrids is compared with the cases of in phase and out of phase poloidal phasing. As expected, the best case corresponds to $\Delta\Phi_{\text{pol}} = 0^\circ$, i.e. the currents flowing in phase in the top and bottom triplets of the same pair. The worst case occurs when these currents are out of phase. For

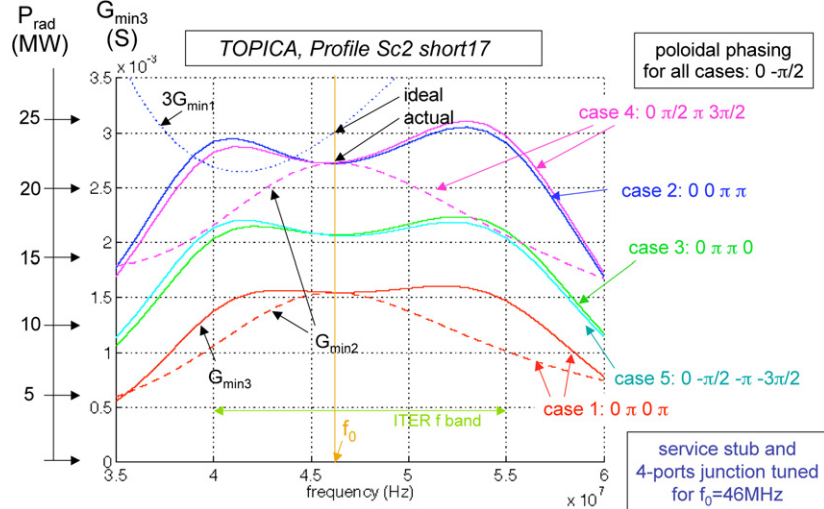


Figure 6. Effective mean minimum conductance $G_{\min 3}$ for five toroidal phasing cases using the plasma profile ‘Sc2 short 17’. $G_{\min 2}$ is given for comparison for cases 1 and 4 and $3G_{\min 1}$ for case 2. The corresponding radiated power scale per antenna array for $|V_{\max 3}| = 45$ kV is given on the left side.

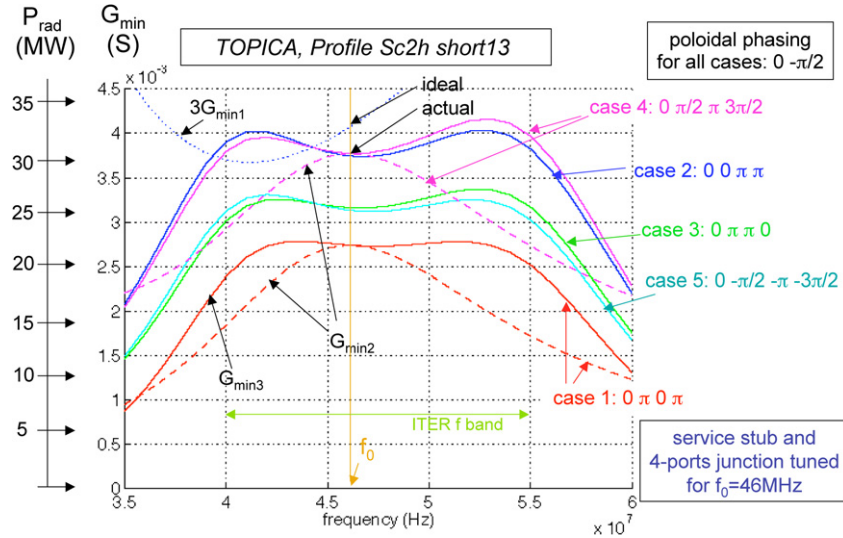


Figure 7. Same as figure 6 but for the plasma profile ‘Sc2h short 13’.

the triplet pair fed by the hybrids the best choice is the $0 - \pi/2$ phasing leading to performances close to the $\Delta\Phi_{\text{pol}} = 0^\circ$ one. For current drive phasing, the influence of the choice of the sign of poloidal and toroidal phasing is striking (see figure 14): a factor two of power capability is expected for current drive depending on the chosen toroidal and poloidal phasing.

3.5. Questions resulting from this analysis

Two results could be considered as particularly surprising, or at least requiring some further physical interpretation:

- (i) The large difference of coupling between the different toroidal phasing cases which is furthermore accentuated from one plasma density profile to another;
- (ii) The asymmetry of coupling for $\Delta\Phi_{\text{pol}} = \pm 90^\circ$.

Both results have important practical implications for ITER as they concern the right choice of connection of each poloidal

pair of triplet to the hybrids or the choice of the co- or counter-direction for optimum current drive coupling.

These issues will be taken up in the next section by means of the simplified, fast coupling code ANTITER II, which will also be used to investigate the contribution of less desirable coaxial and surface modes to the coupling and the influence of edge plasma density profile modifications on the coupling. The ANTITER II code itself is presented in detail in the appendix.

4. Comparative study and furthering the understanding by means of the semi-analytical coupling code Antiter II

4.1. ITER antenna model used for ANTITER modelling

The fast code Antiter II describes the antenna in planegeometry by an array of boxes recessed in the metal wall,

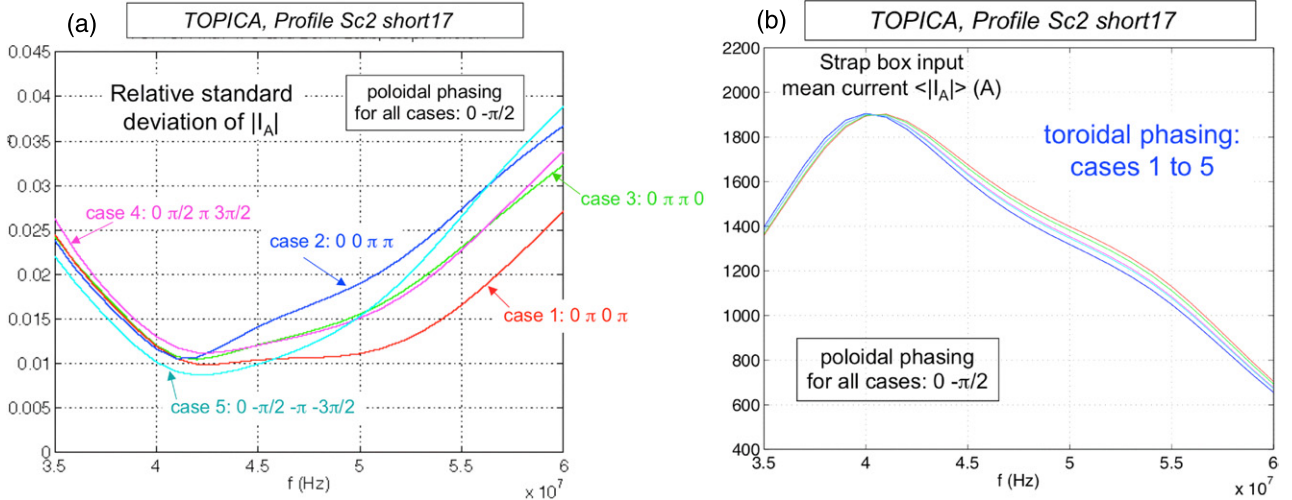


Figure 8. (a) Relative standard deviation of the amplitude of the 24 strap box input currents $|I_A|_i$ ($i = 1, \dots, 24$) using the same $|V_{max3}|$ in the eight feeding lines of the antenna plug and for all toroidal phasing cases. (b) Mean strap box input current amplitude $\langle |I_A| \rangle$ versus frequency for all phasing cases when $|V_{max3}| = 45$ kV.

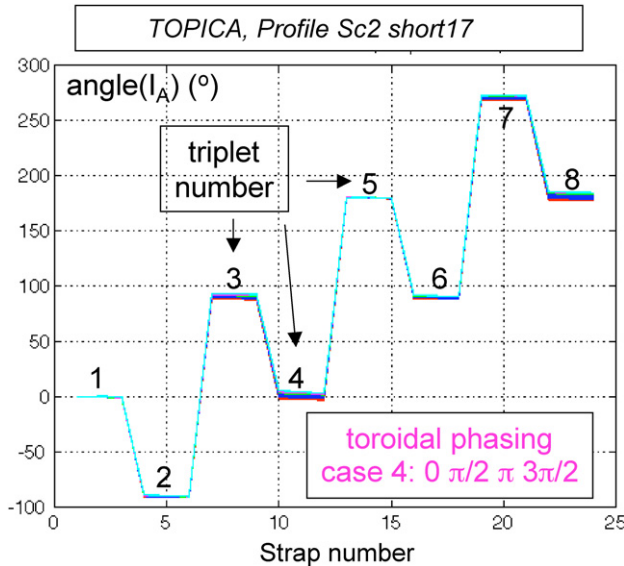


Figure 9. Traces of the phasing of the 24 strap boxes input current I_{Ai} for a current drive case ($\Delta\Phi_{pol} = -90^\circ$) when the phase difference between the triplets is imposed by $V_{max3,j}$ ($j = 1, \dots, 8$). Please note that what is presented is a superposition for each megahertz within the frequency band $35 < f < 60$ MHz. The I_{Ai} phase difference of the three straps in each triplet is negligible.

each box being excited by a thin radiating strap. On the box apertures the Fourier series expansion of the components of the tangential fields inside the box is matched with the $\exp(-i\omega t + ik_z z + ik_y y)$ Fourier integral expansion in the outside medium. Full details of the code are given in the appendix. The modelling of one box facing the inhomogeneous plasma is shown in figure 15 whereas the full ITER strap boxes array is shown by means of the strap box wall apertures in figure 16. As explained in appendix A1, an array tilting angle α of 15° with respect to the total magnetic field B_0 is used. This value corresponds to the slope of B_0 used in TOPICA. The strap, strap box and array dimensions of the

ANTITER simplified geometry are those of the design, except that in ANTITERII the strap thickness is zero and the straps are assumed perpendicular to B_0 but located at the mid-strap position of the actual design.

For the plasma description, a single species deuterium plasma is considered and a constant toroidal magnetic field such that $f = 2f_{cD}$ is assumed. Right-handed rectangular axes with the z -axis along the total steady magnetic field B_0 and the x -axis going outwards of the plasma are chosen.

Instead of the Sc2 short17 density profile, we use an exponentially decaying profile of seven decay lengths $l_{SOL} = 2.4$ cm (from a bulk density of 10^{20} m^{-3} to an edge density of $9.1 \times 10^{16} \text{ m}^{-3}$: see figure 17(a)), after having ascertained that the coupling is nearly identical. The distance separatrix mid-strap is 23 cm. Antenna loading is described by the coupling to the fast magnetosonic wave. Single-pass absorption is assumed in the homogeneous plasma bulk. Figure 17(b) shows the corresponding contour plot of k_\perp^2 (k_\perp is the perpendicular wavenumber of the fast magnetosonic wave) as a function of the density and of $|k_z|$ where the locations of the wave cut-off (for $k_y = 0$) and of the wave resonance are indicated. The former locus is given by $(\omega_{pi}^2)_{CO,k_y=0} = (k_z^2 - k_0^2)(\omega_{ci}^2 \pm \omega\omega_{ci})/k_0^2$ and the resonance density by $(\omega_{pi}^2)_{res} = (k_z^2 - k_0^2)(\omega_{ci}^2 - \omega^2)/k_0^2$. The cut-off densities when $k_y \neq 0$ are obtained from $k_\perp^2(\omega_{pi}^2, \omega, \omega_{ci}, k_z^2) - k_y^2 = 0$. The integration through the resonance is obtained by locally adding collision damping. The absorbed power by this resonance remains very low for our conditions [17].

4.2. Constitutive elements to obtain the active power absorption

In appendix A7 it is shown that the total active radiated power is given by

$$2P_{rad} = 1/(4\pi^2\omega\mu_0)\text{Re} \left\{ \iint |E_y|^2 / \xi_0^* dk_z dk_y \right\}, \quad (1)$$

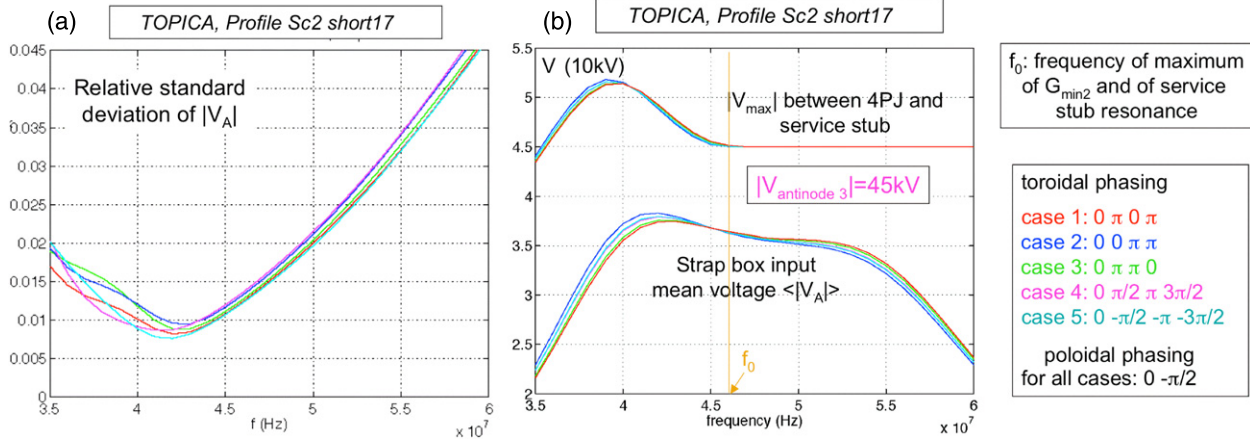


Figure 10. (a) Relative standard deviation of the amplitude of the 24 strap box input voltages $|V_A|_i$ ($i = 1, \dots, 24$) using the same $|V_{max3}|$ in the eight feeding lines of the antenna plug and for all toroidal phasing cases. (b) Mean strap box input voltage amplitude $\langle |V_A| \rangle$ versus frequency for all phasing cases when $|V_{max3}| = 45$ kV. The corresponding maximum voltage between 4PJ and service stub is also shown.

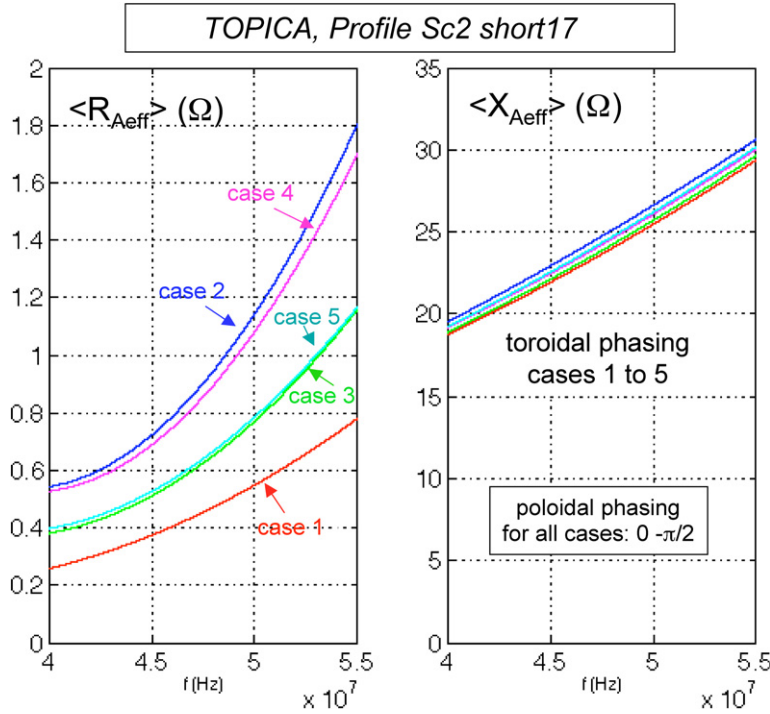


Figure 11. Mean effective resistance $\langle R_{Aeff} \rangle$ and reactance $\langle X_{Aeff} \rangle$ at the input of the strap boxes for all phasing cases.

where $|E_y(k_z, k_y)|^2$ is the excitation function of the array at the wall plane ($x = 0$) in the k_y, k_z space and $1/\xi_0$ is the surface admittance at the box output. The latter quantity is independent of the antenna phasing. Figure 18 shows a contour plot of the normalized surface conductance $Re(1/\xi_0(k_y, k_z))$ at $f = 46.5$ MHz. One notes that this surface admittance is even in k_z but not in k_y : the coupling to the plasma is the same for $\pm|k_z|$ but is different for $\pm|k_y|$. If the magnetic field direction is reversed, the surface admittance remains the same provided the sign of k_y is also reversed. Figure 18 also displays the large contribution occurring for $|k_z| \sim k_0$, due to the coaxial [18] and surface modes [17, 19]. The coaxial modes correspond to TEM/z or TE/z electromagnetic waves propagating between the tokamak wall and the plasma column, which plays the role

of a lossy metal wall. Their dispersion relation is $k_z^2 + k_y^2 \cong k_0^2$. The surface modes are waves guided along the plasma edge for positive $k_y > k_0$ and $|k_z| \sim k_0$. These modes lead to power deposition in the SOL and wall region. In the region $|k_z| > k_0$ corresponding to bulk plasma absorption, the surface conductance is larger for positive k_y values.

The absorbed power depends also on the spectral excitation function in $x = 0$ expressed by $|E_y(k_z, k_y)|^2$. This function selects, depending on the array phasing, the k_z, k_y spectral parts which significantly contribute to the coupled power. The contours of $|E_y(k_z, k_y)|^2$ for one heating and one current drive phasing with the best quadrature poloidal phasing $\Delta\Phi_{pol} = -90^\circ$ are shown in figure 19. The cases without ($\alpha = 0$) and with ($\alpha = 15^\circ$) antenna tilting with respect to B_0 are compared.

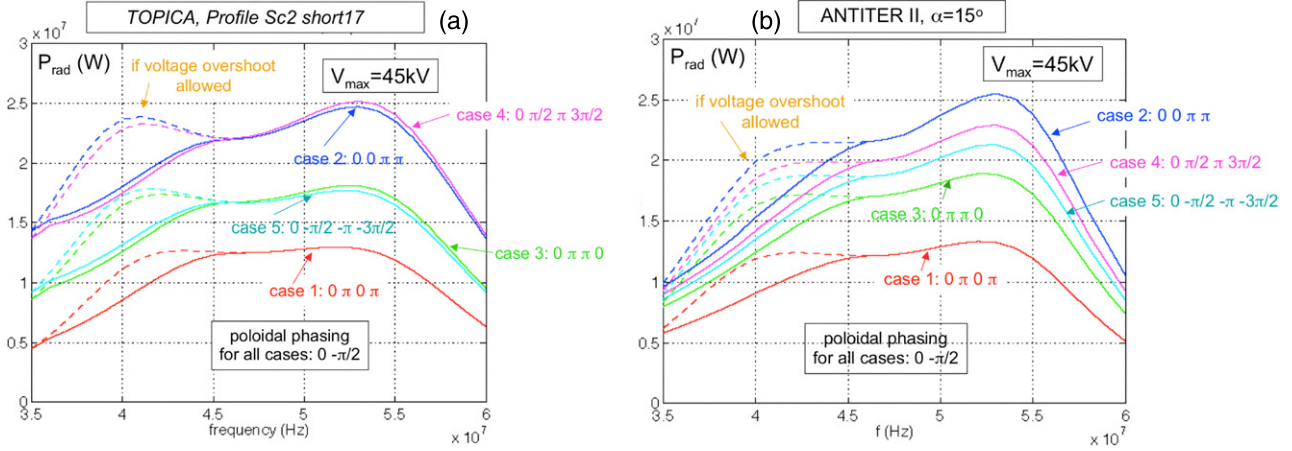


Figure 12. (a) Power capability per antenna array versus frequency as predicted by TOPICA (profile Sc2 short17) if the maximum voltage is limited everywhere to 45 kV. For comparison the case with $|V_{max}| = 45$ kV, allowing a voltage overshoot at low frequency, is also shown. (b) Corresponding power capability predicted by ANTITER II, for an antenna tilting of $\alpha = 15^\circ$.

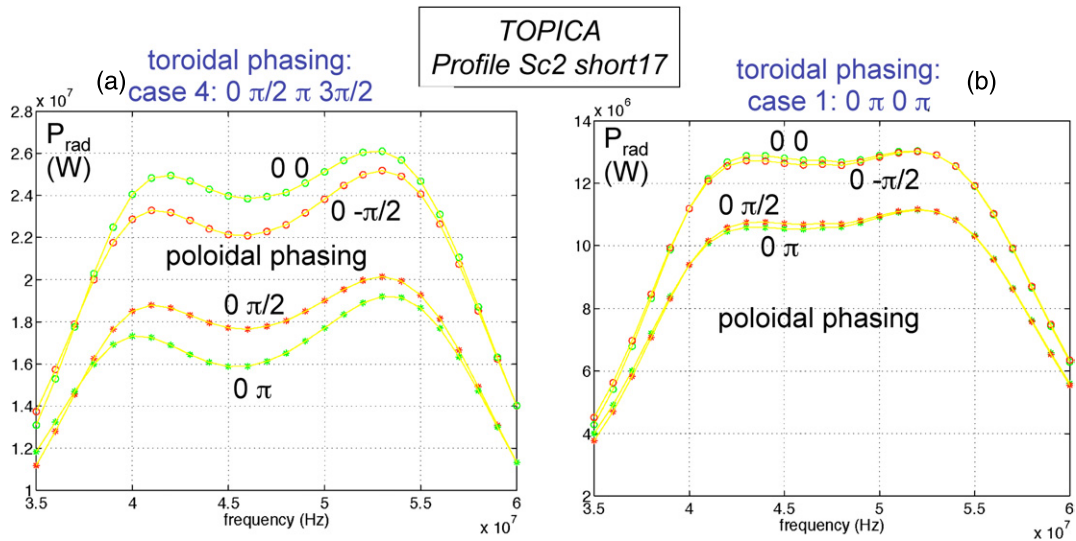


Figure 13. Effect of the poloidal phasing on the power capability per antenna array of (a) a current drive case and (b) a heating case.

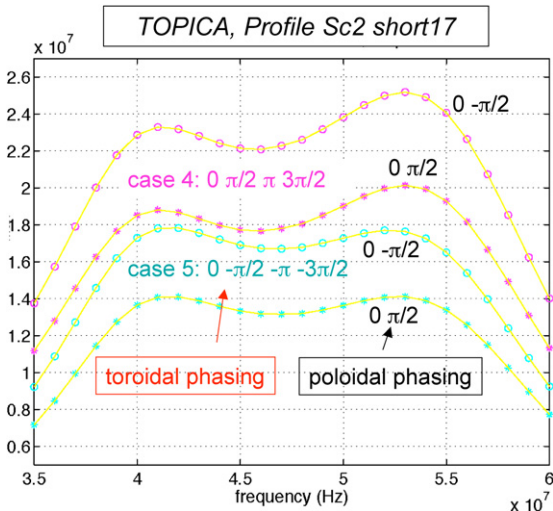


Figure 14. Effect of the toroidal and poloidal phasings on the power capability per antenna array for the current drive phasings.

4.3. Effects of surface admittance and spectral excitation function on coupling properties

- The real part of the surface admittance leads to a larger coupling to the plasma for $k_y > 0$, i.e. for waves with phase velocity towards $y > 0$. This explains a larger coupling for a poloidal phasing $0 -\pi/2$ than for $0 +\pi/2$. The coupling to coaxial modes occurs for $|k_z| < k_0$ with a surface modes contribution for $k_y > 0$ [17].
- Because of the evenness of the excitation in k_z , current drive with phase velocity towards $z < 0$ (case 4: $0\pi/2\pi 3\pi/2$) leads to the same coupling as phasing with phase velocity towards $z > 0$ (case 5: $0 -\pi/2 -\pi -3\pi/2$) in the absence of poloidal magnetic field (figure 19, left plots).
- However, the effective poloidal and toroidal phasings imposed by the spectral excitation function change on account of the poloidal field, as shown in figure 19 (right plots).

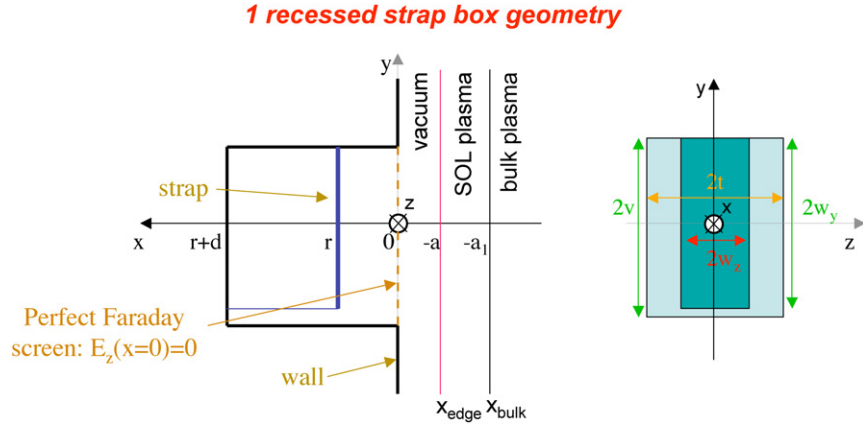


Figure 15. Modelling by ANTITER II: geometry of each recessed strap box in the wall, in front of a plasma with an inhomogeneous edge layer.

View of the strap box apertures in the wall

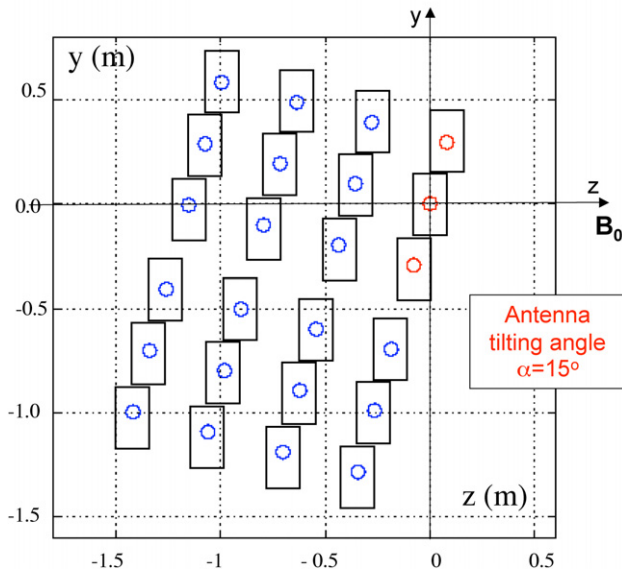


Figure 16. Modelling by ANTITER II: view of the strap box apertures of the complete array, simulating an antenna tilting of 15° with respect to B_0 .

4.4. Comparison TOPICA-ANTITER for the evolution of $G_{\min 3}$ versus $\Delta\Phi_{\text{pol}}$

TOPICA results. Figure 20 shows the large variation of $G_{\min 3}$ versus $\Delta\Phi_{\text{pol}}$ for the considered toroidal phasing cases. $G_{\min 3}$ is maximum for, depending on the case, $\Delta\Phi_{\text{pol}} \approx -30\text{--}50^\circ$, i.e. corresponding to an *upward* (i.e. towards $y > 0$) poloidal phase velocity in front of the antenna [9]. The current drive phasing cases 4 and 5 exhibit a large difference in the amplitude of $G_{\min 3}$ for all $\Delta\Phi_{\text{pol}}$ values.

Please note that in [9] the matrix is computed (i) with directions of the total magnetic field and of the plasma current that are opposite to the ITER baseline, shown in figure 3 and (ii) with an $\exp(+i\omega t)$ time dependence, whereas $\exp(-i\omega t)$ is assumed in this paper. Appropriate corrections were made when transposing the Topica results.

ANTITER II without antenna tilting. As seen in figure 21(a), $G_{\min 3}$ is also maximum for $\Delta\Phi_{\text{pol}} \approx -30\text{--}40^\circ$ and a maximum excitation for $k_y \approx +0.5 \text{ m}^{-1}$. The poloidal phasing $0\text{--}\pi/2$ leads to a better coupling than $0\text{--}\pi/2$. In agreement with TOPICA this corresponds to a predominant *upward* poloidal phase velocity. Note also that, opposite to TOPICA results, the current drive cases 4 and 5 have the same $G_{\min 3}$ because the surface conductance is even in k_z .

ANTITER II with 15° tilting. The effective phasing parallel (along the z -axis) and perpendicular (along the y -axis) to B_0 seen by the plasma is different from the toroidal and poloidal strap current phasing. This is due to the antenna tilting with respect to B_0 . It produces a difference between the current drive cases 4 and 5 because the additional poloidal phasing in the y -direction introduced by the tilting is different for both cases. The resulting effect is shown in figure 21(b). Contrarily to TOPICA the same difference of $G_{\min 3}$ is not maintained for all poloidal phasing values and the tilting effect is smaller in ANTITER II. There is only a slight effect of the tilting on the heating cases.

A global comparison of the performances predicted by TOPICA and ANTITER can be found from the juxtaposition of figures 12(a) and (b). One sees that ANTITER II, in spite of the simplicity of its geometry, provides not only a good qualitative agreement with TOPICA but also a fair quantitative one.

4.5. Coaxial and surface mode excitation

In section 4.2 and figure 18 it was noted that coaxial and surface mode occur for $|k_z| \lesssim k_0$. The monopole toroidal phasing (0 0 0 0) leads to the optimal excitation of this low $|k_z|$ spectrum resulting, due to the coaxial and surface mode excitation, in a much larger $G_{\min 3}$ value than for the other phasing cases. This is shown versus $\Delta\Phi_{\text{pol}}$ in figures 22(a) and (b), respectively, for TOPICA and for ANTITER. In ANTITER the contribution of the coaxial and surface modes can be removed by letting $k_0 \rightarrow 0$ in the field description (i.e. quasi-static approach) [18, 19]. In figure 22(b) the comparison of $G_{\min 3}$ with and without the contribution of these modes is shown for the different toroidal phasing cases. For each case the bottom curve gives the antenna coupling without the coaxial modes

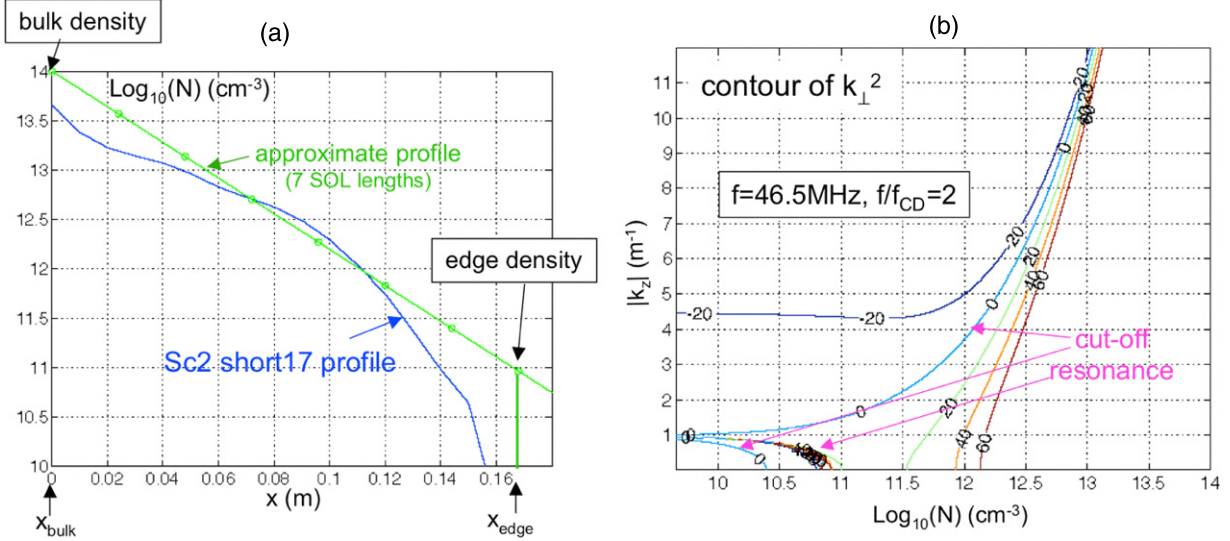


Figure 17. (a) Profile ‘Sc2 short17’ and its approximate exponential density profiles used in ANTITER for the SOL description. (b) Contour plot of k_{\perp}^2 versus plasma density and $|k_z|$ ($f = 46.5$ MHz, $f/f_{CD} = 2$, deuterium plasma).

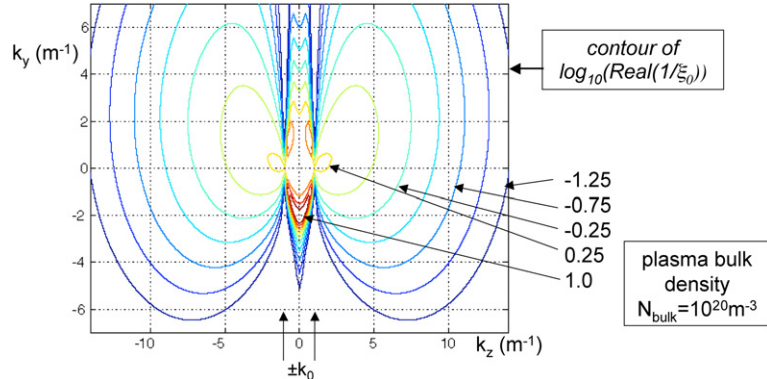


Figure 18. Contour plot of the surface conductance in ANTITER at $x = 0$ (plasma side) versus k_z and k_y for the approximate plasma profile of figure 16(a).

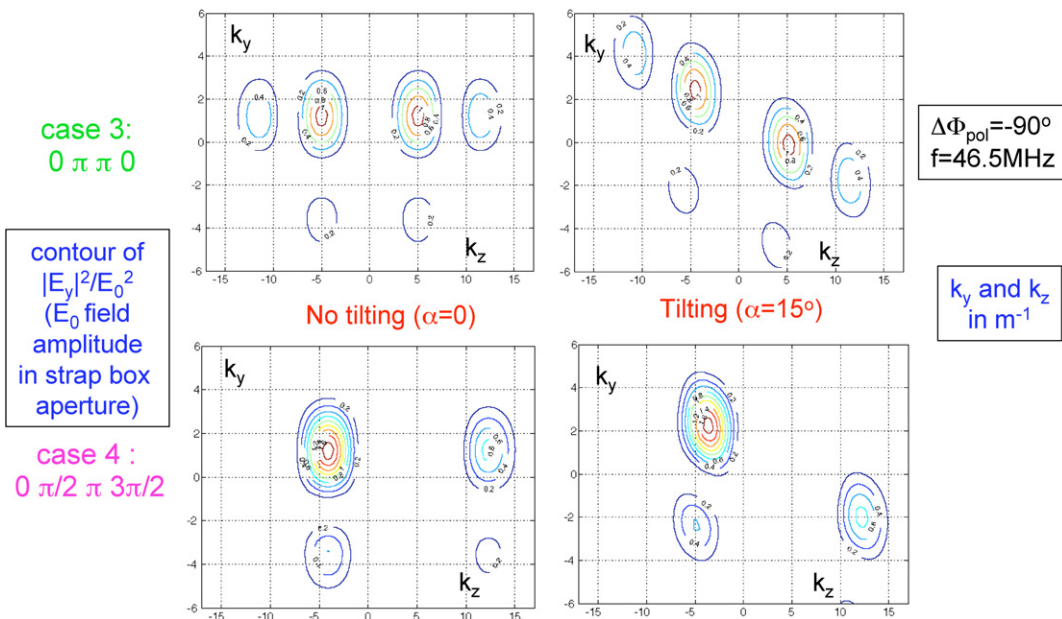


Figure 19. Normalized spectral excitation function versus k_z and k_y for one heating case and one current drive case.

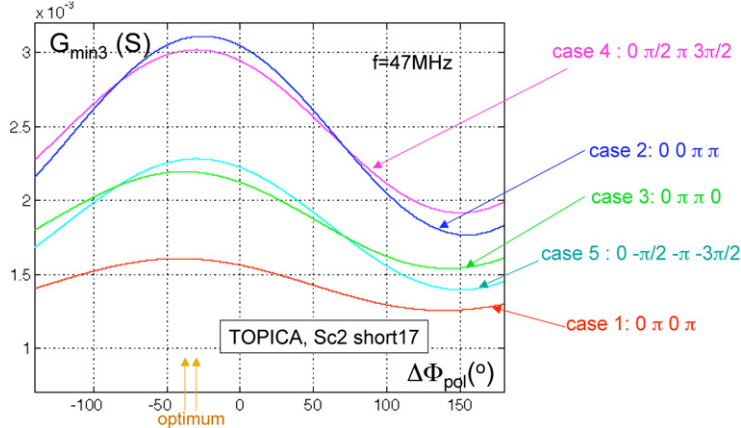


Figure 20. Evolution as a function of the poloidal phasing angle $\Delta\Phi_{\text{pol}}$ of the effective averaged minimum conductance $G_{\min 3}$ for five toroidal phasing cases as predicted by TOPICA for the Sc2 short17 plasma profile.

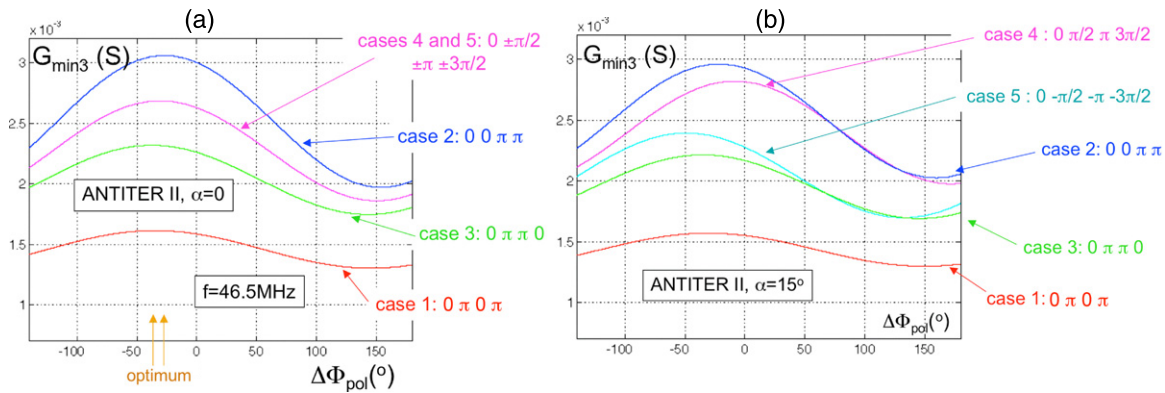


Figure 21. Same as figure 20 but computed by ANTITER II with the approximate profile of figure 16(a), (a) without antenna tilting, (b) with an antenna tilting $\alpha = 15^\circ$.

contribution and its difference with the top curve corresponds to the coaxial modes contribution. It is important only for the monopole phasing and its relative contribution to the other cases is much smaller (only a few per cent).

4.6. k_y and k_z power spectra

Using equation (A.13), we obtain figures 23 and 24, showing the radiation resistance spectra (see appendix A7) for the considered toroidal phasing cases (except monopole) with $\Delta\Phi_{\text{pol}} = -90^\circ$ and $\alpha = 15^\circ$. As expected from the analysis of section 4.3 and figure 19, each phasing selects narrow region(s) in the k_z , k_y plane which are significantly contributing to the loading. The most contributing $|k_z|$ of each case is indicated in figure 23. The k_z spectrum is weakly depending on $\Delta\Phi_{\text{pol}}$ as shown in figure 25(a) from the superimposed k_z spectra for $-140 < \Delta\Phi_{\text{pol}} < 180^\circ$ (one curve each 10°) corresponding to the $\Delta\Phi_{\text{pol}}$ scan of figure 21(b). The asymmetry in k_z with respect to $k_z = 0$ of the heating cases 1, 2 and 3 is due to the tilting angle which induces a current drive effect even on the heating phasings. The effect of tilting is larger on the effective poloidal phasing than on the toroidal one and larger for current drive phasing than for the heating ones. With antenna tilting symmetry occurs between the two current drive cases: the results of one case are identical to those of the other case if the sign of the tilting angle α is reversed. An example of

the dependence of the k_y spectrum on the tilting angle and on $\Delta\Phi_{\text{pol}}$ is shown for case 1 in figure 26.

The strong contribution of the coaxial and surface modes to the monopole coupling for $|k_z| \approx k_0$ is illustrated in figure 25(b). Their contribution to the other phasing cases is much smaller, as can be seen in figure 23 and 25(a). This is due to the low corresponding value of the spectral excitation function for $|k_z| \approx k_0$ as shown for phasing cases 3 and 4 in figure 19.

4.7. Consequences for ITER

- (1) The optimum heating coupling requires a preferential excitation of $k_y > 0$ (but close to $k_y = 0$), i.e. of slight poloidal phase velocity towards $y > 0$. This corresponds for ITER to upward phase velocity (also concluded in [20, 21]).
- (2) The best coupling current drive case (case 4: $0 \pi/2 \pi 3\pi/2$ toroidal phasing) corresponds to excitation of negative k_z , i.e. phase velocity towards $z < 0$. This will accelerate electrons towards $z < 0$ and therefore produce co-current drive (as also pointed out in [20, 21]).
- (3) The monopole phasing should be avoided for plasma heating but can be of interest for wall conditioning purposes.

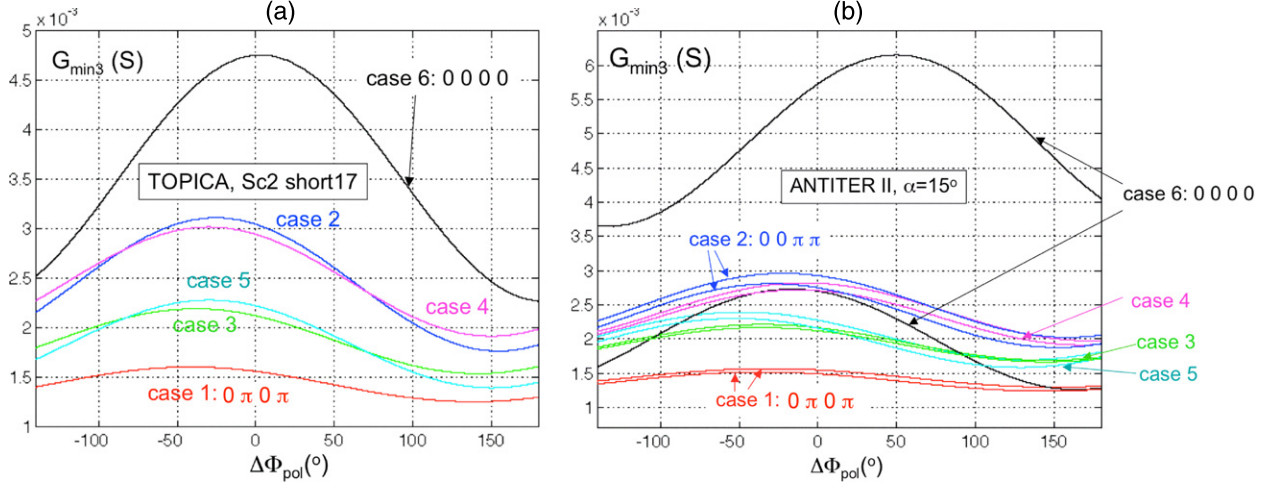


Figure 22. (a) TOPICA: Same as figure 20 with in addition the curve of the monopole phasing. (b) ANTITER II: same as figure 21(b) with and without the coaxial and surface modes contribution including the case of the monopole phasing. The bottom curve of each case is the one without the coaxial and surface modes contribution.

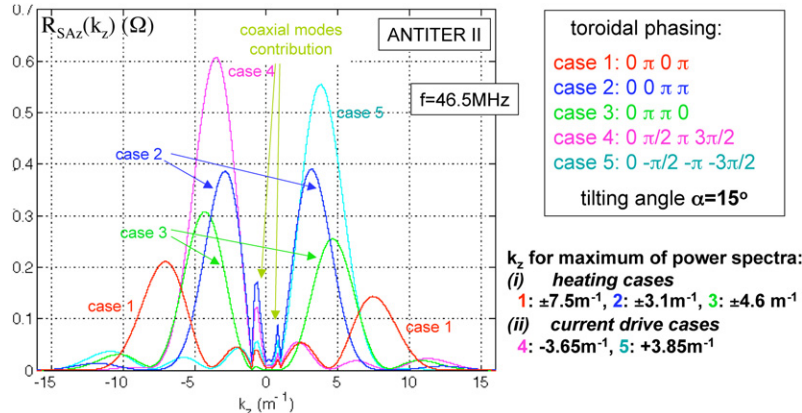


Figure 23. k_z spectra of the mean radiation resistance for different toroidal phasing cases and for $\Delta\Phi_{\text{pol}} = -90^\circ$.

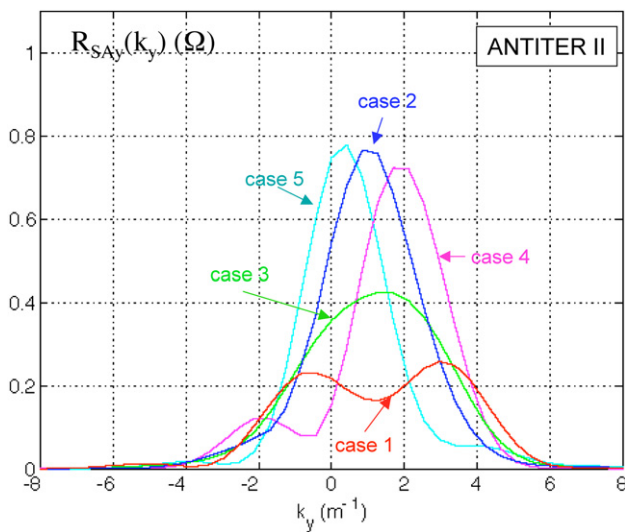


Figure 24. k_y spectra of the mean radiation resistance for the cases shown in figure 23.

4.8. Study of the relative change in coupling of the different toroidal phasing cases as a function of the density profile between bulk plasma and antenna

In this section we use ANTITER II to make numerical experiments on the sensitivity of the coupling of the different heating and current drive cases to the SOL plasma profile modifications. In all these simulations, it is assumed that the mid-plane of the antenna straps is retracted 0.06 m within the ITER wall.

4.8.1. Effect of replacing a part of the SOL density profile in front of the antenna by vacuum. We assume a constant distance bulk plasma mid-strap $a_1 = 0.23$ m, a constant density decay length $l_{\text{SOL}} = 2.4$ cm (as defined in section 4.1 and figure 17(a)) but we interrupt, as shown in figure 27(a), the decaying profile at a variable position x_{edge} such that the edge density varies from 8×10^{19} down to $1.2 \times 10^{16} \text{ m}^{-3}$. In this figure $x_{\text{edge}} = 0$ corresponds to a density step function at the start of the bulk plasma (i.e. \sim the separatrix position). The evolution of the coupling, expressed by $G_{\min 3}$, as a function of x_{edge} for the different phasing cases is given in figure 27(b). In the figure the value of x_{edge} corresponding to N_{edge} equal

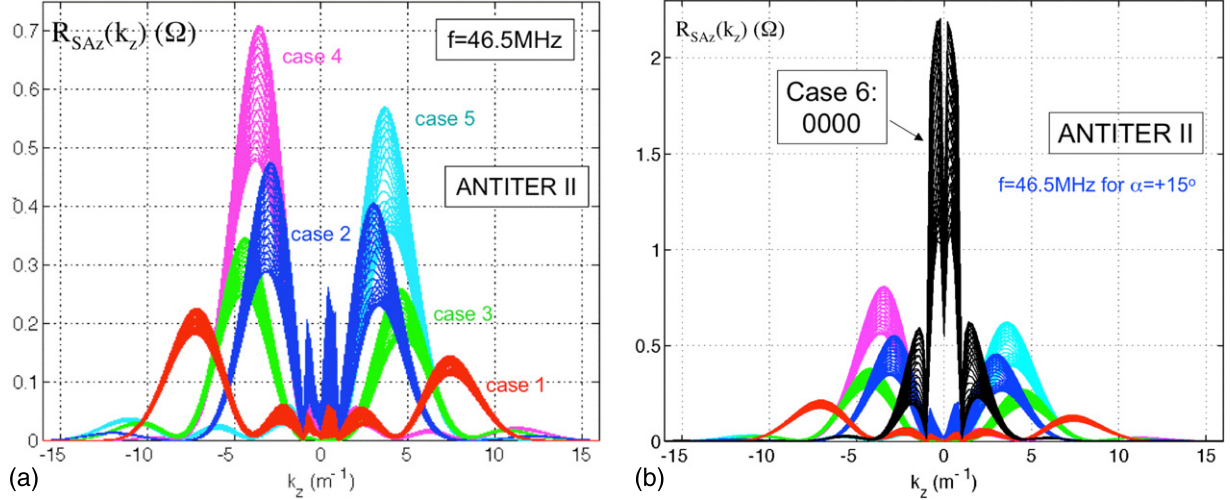


Figure 25. (a) Superimposed traces of the k_z spectra of the mean radiation resistance for $-140^\circ \leq \Delta\Phi_{\text{pol}} \leq 180^\circ$ (1 curve each 10°). (b) Same as (a) with in addition the case of the monopole phasing showing the large contribution of coaxial and surface modes.

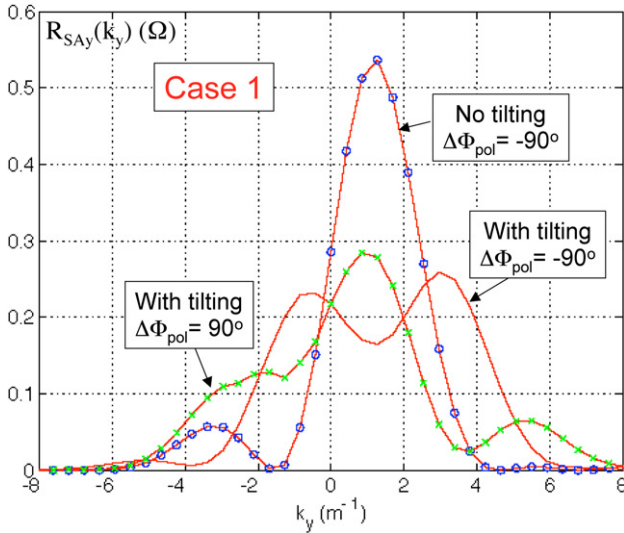


Figure 26. Examples of the effect of tilting and poloidal phasing on the k_y spectra of the mean radiation resistance (case 1 of toroidal phasing: $0\pi 0\pi$).

to the cut-off density N_{CO} of the heating cases 1, 2 and 3 is indicated. Each value of N_{CO} is obtained from $k_{\perp}^2 - k_y^2 = 0$ for the $|k_{zM}|, k_{yM}$ values corresponding to the maximum of the radiation resistance spectra shown in figure 23. One observes that the loading only decreases by 5–12% if the plasma of density lower than N_{CO} is replaced by vacuum and does not decrease at all if the plasma of density lower than $N_{\text{CO}}/3$ is removed. This indicates that the presence of blanket modules acting as limiters near the antenna array will only significantly reduce the coupling if they intercept SOL plasma density equal to or larger than the N_{CO} value corresponding to the chosen phasing. This also indicates that filling (e.g. by gas puff) the vacuum layer with plasma of density lower than N_{CO} will only marginally improve the coupling.

The coupling ratio between cases 2 ($00\pi\pi$) and $1(0\pi 0\pi)$ varies from 1.2 to 1.8 when the decreasing density plasma fills the gap bulk plasma–antenna

4.8.2. Scan of density decay length l_{SOL} . We assume a constant distance bulk plasma mid-strap $a_1 = 0.23 \text{ m}$ and a density decay over $7 l_{\text{SOL}}$. Therefore, the distance plasma edge mid-strap $a = a_1 - 7l_{\text{SOL}}$. The bulk plasma density is 10^{20} m^{-3} and the edge density $9.1 \times 10^{16} \text{ m}^{-3}$. The resulting evolution of $G_{\min 3}$ for the different phasing cases is given in figure 28 together with the value of l_{SOL} for which there is a same distance cut-off density (N_{CO})-strap, taken equal to 15 cm, for the three heating cases. This shows, as in the previous section 4.8.1, that long density decay lengths increase the coupling and the coupling ratio of the different cases. It also indicates that the difference between the $G_{\min 3}$ values of the three heating cases is reduced when l_{SOL} is decreased. It should be noted, however, that when the cut-off densities for the three phasings are at the same distance from the antenna, the coupling order is actually reversed.

4.8.3. Sensitivity of the power capability to the plasma position. In this numerical experiment the complete plasma profile is displaced with respect to the antenna. The density decay length $l_{\text{SOL}} = 2.4 \text{ cm}$ (approximation of Sc2 short17 profile) is maintained with a number of $9 l_{\text{SOL}}$ and the distance plasma edge-strap a is varied from 0 to 10 cm. Therefore the distance plasma bulk mid-strap is $a_1 = a + 0.216$. The bulk plasma density is 10^{20} m^{-3} and the edge density $1.23 \times 10^{16} \text{ m}^{-3}$. Figure 29 shows that, for a given plasma profile, the dependence of the power capability on the plasma–antenna distance is roughly exponential. This is valid for all heating cases: the power capability varies roughly of 1 dB/2 cm (i.e. 26%/2 cm) for the heating cases 2 ($00\pi\pi$) and 3 ($0\pi\pi 0$) and the current drive cases 4 and 5, of 1.5 dB/2 cm (i.e. 41%/2 cm) for the heating case 1 ($0\pi 0\pi$) and of 0.5 dB/2 cm (i.e. 12%/2 cm) for the monopole case 6 (0000). We have checked that this dependence is still true if l_{SOL} decreases from 2.4 to 1.8 cm. The lower sensitivity of the monopole is interpreted by the large coaxial mode contribution and the larger sensitivity of case 1 by its large $|k_z|$ value. Nevertheless, if we compare the computed coupling decrease with a $\exp(-2\delta p\Delta x)$ dependence on the radial displacement

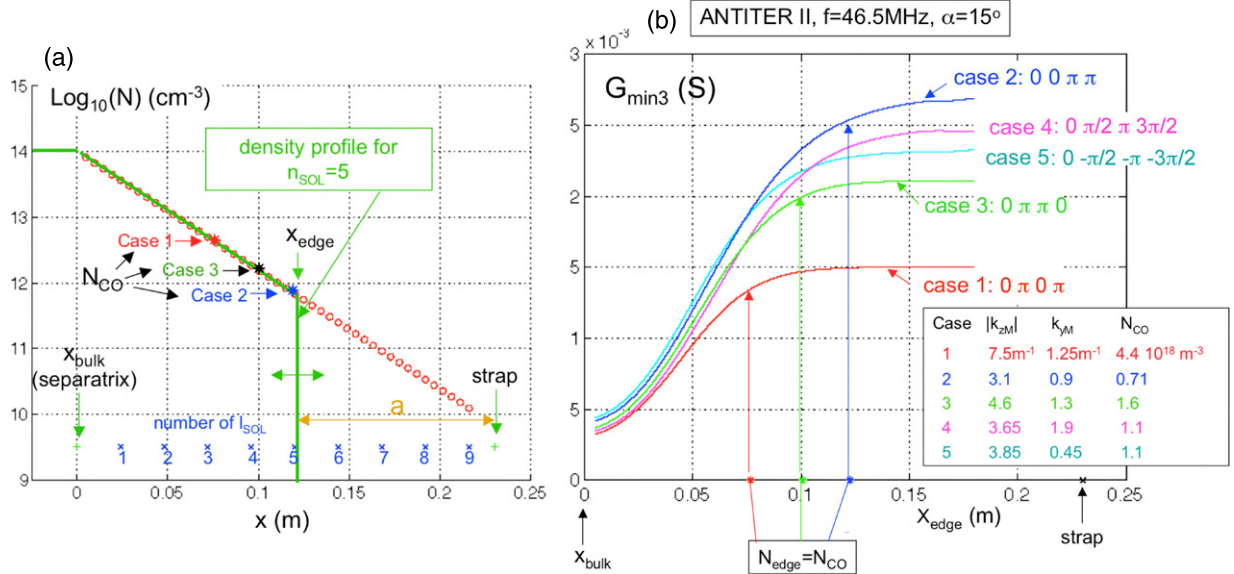


Figure 27. (a) Exponentially decaying plasma profile with $l_{\text{SOL}} = 2.4$ cm interrupted at variable x_{edge} . The distance x_{bulk} mid-strap is 23 cm and there is vacuum between x_{edge} and strap. (b) Evolution of $G_{\min 3}$ for the different toroidal phasing cases as a function of the position of x_{edge} . The value of x_{edge} for which the edge density N_{edge} is equal to the cut-off density N_{CO} of the corresponding heating case is indicated.

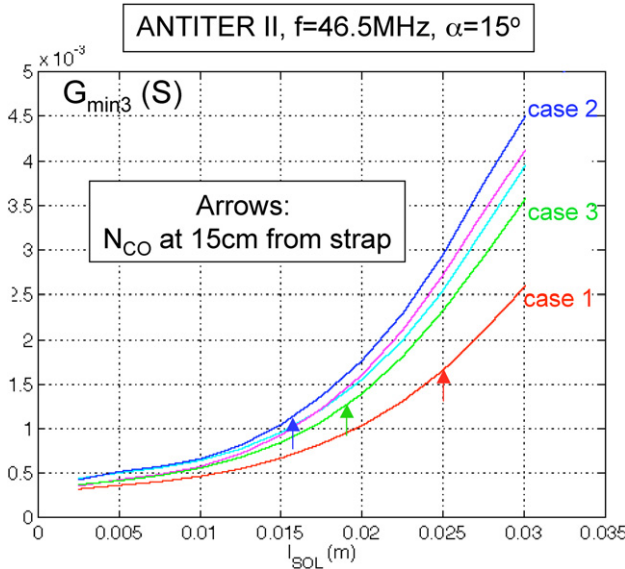


Figure 28. $G_{\min 3}$ versus l_{SOL} for an exponentially decaying profile of $7 l_{\text{SOL}}$. There is a fixed distance bulk plasma-wall of 23 cm. Arrows indicate the l_{SOL} value for which the corresponding N_{CO} density value is at 15 cm from the wall.

Δx (where δ is a fitted parameter and p is evaluated for the $|k_{zM}|$, k_{yM} values of the corresponding case; see table in figure 27(b)) one obtains $\delta \cong 2$ for case 1 (i.e. equal to the decay in vacuum; see section 4.8.4) and larger values for the other cases ($\delta \cong 3$ for case 2, $\delta \cong 2.5$ for case 3 and $\delta \cong 2.75$ for cases 4 and 5).

4.8.4. Sensitivity to the steepness of the density profile near the plasma bulk. For this experiment we assume a density profile with two different decay lengths in the SOL, the first being variable ($0.5 < l_{\text{SOL1}} < 5$ cm) near the plasma bulk and the second constant ($l_{\text{SOL2}} = 2.4$ cm) as depicted in

figure 30(a). The change in l_{SOL} takes place at a fixed density $N_{\text{TO}} = 8 \times 10^{18} \text{ m}^{-3}$. The N_{CO} values corresponding to the heating cases 1, 2 and 3 are indicated in the figure and occur in the part of the density profile with constant l_{SOL2} . We recall that the Sc2 short 17 density profile corresponds approximately to $l_{\text{SOL1}} = 2.4$ cm. The dependence of $G_{\min 3}$ on l_{SOL1} is shown in figure 30(b). A large decrease in l_{SOL1} leads to a significant coupling decrease, even if the plasma bulk moves closer. This is due to large reflection of the incoming wave (refraction-index mismatch) as shown below. Nevertheless, the coupling increases with l_{SOL1} only up to a threshold l_{SOL1} value which is an increasing function of $|k_{zM}|$, on account of a saturation effect due to the competition between the reduction in reflection by the gradient and the increase in distance antenna–plasma bulk. The coupling ratio of the different phasing cases is also an increasing function of l_{SOL1} up to $l_{\text{SOL1}} = 2.5$ cm and after this limiting value it starts to decrease.

The physics of the coupling dependence on the profile can be investigated from the field behaviour between the antenna and the bulk plasma. As explained in section 4.3 the absorbed power is due mainly to a small region \mathfrak{R} of the $|k_z|$, k_y spectrum centred on the $|k_{zM}|$, k_{yM} values leading to maximum absorption. Therefore an approximate expression of equation (1) for the absorbed power can be given by

$$2P_{\text{rad}} = \{A/(4\pi^2\omega\mu_0)\}\text{Re}\{1/\xi_0^*(|k_{zM}|, k_{yM})\}$$

$$\text{with } A = \iint_{\mathfrak{R}} |E_y|^2 d k_z dk_y. \quad (2)$$

The coupling can then be studied from the behaviour of the $|k_{zM}|$, k_{yM} wave component in the inhomogeneous plasma. The coupled active power can also be computed at the boundary of the plasma bulk from the Poynting theorem by $P \propto \{|E_y(x=x_{\text{bulk}})|^2 / \text{Re}(\xi_{\text{bulk}})\}_{k_{zM}, k_{yM}}$ where $\xi_{\text{bulk}}(k_{zM}, k_{yM})$ is the normalized surface impedance $\{E_y/(\omega B_z)\}_{x=x_{\text{bulk}}}$ of the plasma bulk. If the bulk plasma density N_{bulk} is sufficiently large (i.e. $\omega/V_A \gg |k_{zM}|, |k_{yM}|$; V_A : Alfvén velocity of the

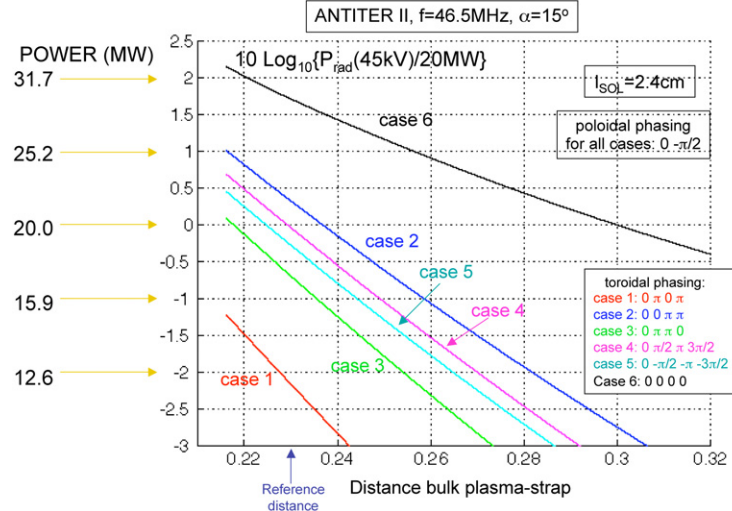


Figure 29. Variation of the power capability per antenna array for $|V_{\max 3}| = 45$ kV (expressed in dB with respect to 20 MW) versus the distance plasma bulk mid-strap for the same exponentially decaying plasma profile ($l_{\text{SOL}} = 2.4$ cm, $9 l_{\text{SOL}}$).

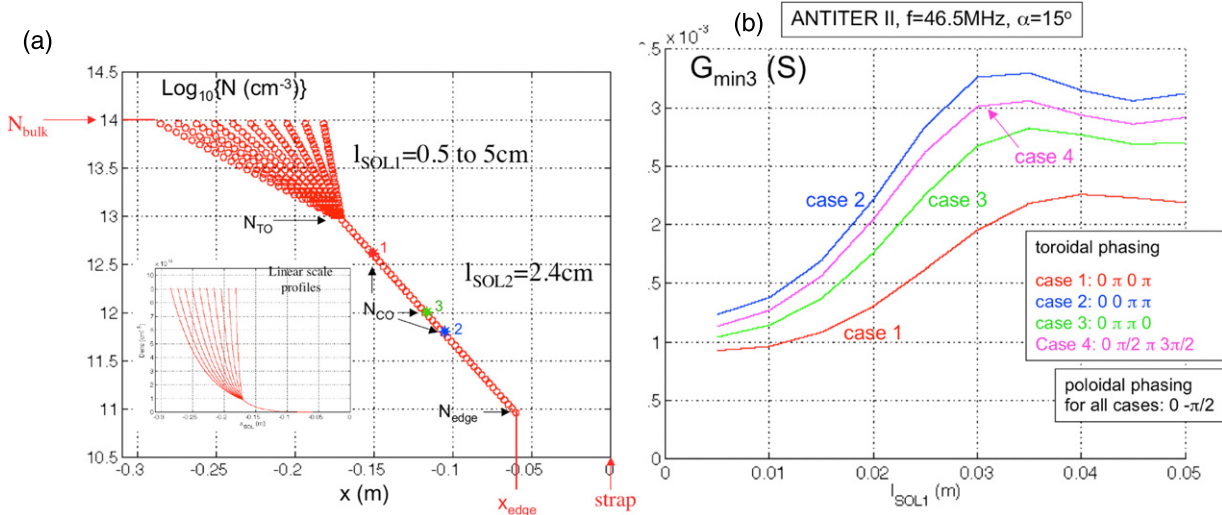


Figure 30. (a) Plasma profile with two density decay lengths: variable l_{SOL1} and constant l_{SOL2} . (b) $G_{\min 3}$ as a function of l_{SOL1} for different toroidal phasing cases.

plasma bulk) we have $\xi_{\text{bulk}} \cong V_A/\omega$ (see appendix A4). For our case ($N_{\text{bulk}} = 10^{20} \text{ m}^{-3}$, $f/f_{\text{cD}} = 2$, $f = 46.5$ MHz) we have $\xi_{\text{bulk}} = 0.0163$ – 0.0167 m, roughly independent of the antenna phasing. Therefore, the E_y amplitude reached at the bulk plasma boundary is a measure of the plasma loading.

Figures 31(a) and (b) compare the $|E_y(|k_z M|, k_y M)|$ evolution from the antenna mouth to the plasma bulk boundary for heating cases 1 and 2 and for $l_{\text{SOL1}} = 3.5$ and 0.5 cm, normalized with respect to its value $|E_{y0}|$ at the antenna mouth ($|E_{y0}|$ is weakly dependent on the considered plasma profiles: 2.3% variation for $0.5 < l_{\text{SOL1}} < 5$ cm). The loading is therefore proportional to the square of $|E_y(|k_z M|, k_y M)|$ at the plasma bulk boundary, i.e. for $x = x_{\text{bulk}}$ of the considered profile. The corresponding field behaviour in three further situations is also shown: (a) ‘vacuum case’ in vacuum (no SOL neither bulk plasma), this case corresponds to the lowest possible k_{\perp} mismatch; (b) ‘bulk plasma case’ with only the SOL plasma being replaced by vacuum and still the bulk plasma at the same position and (c) ‘metal case’ in vacuum with

the bulk plasma boundary replaced by a metal plate, this case corresponds to the highest possible k_{\perp} mismatch (total field reflection). The vacuum field behaviour [18, 22] is expressed by the relations

$$\begin{aligned} |E_y(x)/E_y(0)| &= |\exp(px)| && \text{and} \\ |E_y(x)/E_y(0)| &= |\sinh[p(x - x_{\text{bulk}})]/\sinh(px_{\text{bulk}})|, \end{aligned} \quad (3)$$

respectively, for the ‘vacuum case’ and for the ‘metal case’ with $p = (k_z^2 + k_y^2 + k_0^2)^{0.5}$. Figures 31(a) and (b) show that no special behaviour of the fields appears near the locations of the plasma boundary (N_{edge}), the wave cut-off (N_{CO}) and turnover density (N_{TO}). The coupling depends on the complete density profile. A steeper profile after the cut-off density leads to larger reflection and decreases the coupling: the field behaviour then becomes closer to the ‘bulk plasma case’ which follows the ‘metal case’ trajectory except near $x_{\text{SOL}} = x_{\text{bulk}}$. When l_{SOL1} increases, the field behaviour becomes closer to the ‘vacuum

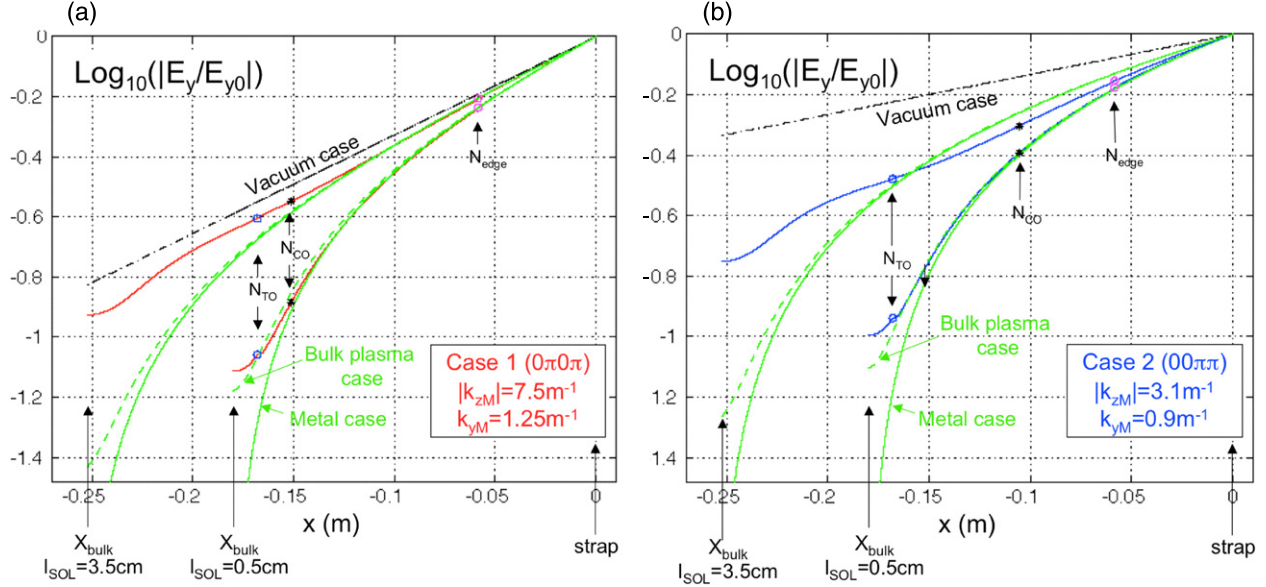


Figure 31. $|E_y/E_{y0}|$ field evolution between the strap and the bulk plasma for k_{zM} and k_{yM} selected by the considered phasing: (a) for case 1 ($0\pi0\pi$), (b) for case 2 ($00\pi\pi$). The curves corresponding to the ‘vacuum’, ‘metal’ and ‘bulk plasma’ cases are added for comparison.

case’ and $|E_y(x = x_{\text{bulk}})|$ increases. The room for this increase is narrower when $p = (k_{zM}^2 + k_{yM}^2 + k_0^2)^{0.5}$ is larger. This is seen in figures 31(a) and (b) and results from relations (3). It explains the larger relative increase in cases with lower p value observed with a constant distance strap=bulk plasma when the transition vacuum-plasma bulk is more progressive as appears in figures 27(b), 28 and 30(b). Let us also note that for a progressive transition the field behaviour is closer to the ‘vacuum case’ for large p values.

Our analysis shows that for small l_{SOL1} the coupling can be improved if the combination of l_{SOL2} , N_{TO} and N_{edge} decreases sufficiently the distance cut-off density–antenna and provides a more gradual density increase towards the steep gradient region. If gas puff would be used to increase the H-mode coupling, it must provide density above the cut-off one as close as possible to the antenna.

5. Conclusions

The rf performance of the proposed ITER ICRF system has been evaluated in the ITER frequency band by means of the antenna array impedance matrix provided by the TOPICA and 4-port junction matrices found by MWS and confirmed by the semi-analytical code ANTITER II. From this analysis we conclude:

- The broadbanding effect of the service stub, studied for one triplet, is maintained for the complete array and for any toroidal and poloidal phasing of the triplets and is not significantly affected by modification of the plasma profile.
- The present design of the 4-port junction is close to the ideal one.
- For a given anti-node voltage of the eight feeding lines the radiated power capability remains roughly constant in the whole frequency band.

- A voltage overshoot occurs in the line section between the 4-ports junction and the service stub in the lower part of the frequency band (<46 MHz). If the maximum voltage in this section cannot exceed the anti-node voltage of the feeding lines the above-mentioned power capability will be reduced in this part of the frequency band up to 30% at 40 MHz.
- The feedback control of the anti-node voltage of the eight feeding lines by means of the matching system allows a precise control of the current distribution of the strap array for any phasing and the plasma profile.
- The power capability is significantly dependent not only on the plasma density profile but also on the toroidal and poloidal phasing. To exceed a power capability of 20 MW per antenna of radiated power, in the upper part of the frequency band, with a separatrix–wall distance of 17 cm and a not too optimistic plasma edge density profile, the system voltage stand-off must be 45 kV and well chosen combinations of toroidal and poloidal phasing are needed.
- The fast semi-analytical code ANTITER II allows us to readily study the underlying physics and to perform numerical experiments. A comparison with the TOPICA predictions shows similar qualitative and even quantitative results and allows explaining the strong dependence of coupling on phasing. The poloidal steady magnetic field has to be taken into account to describe the TOPICA results with current drive toroidal phasing.
- The observed asymmetry of coupling of the different toroidal cases with respect to zero poloidal phasing is due to the plasma gyrotropy. The coupling is larger for waves launched with poloidal phase velocity towards $y > 0$ (i.e. going upwards for the ITER B -direction). The connection to the hybrids must therefore be accordingly chosen.
- The difference in coupling between the two current drive poloidal phasings is interpreted as due to the antenna tilting with respect to B due to the poloidal magnetic field. This produces for the plasma an effective phasing

- different from the applied toroidal and poloidal current phasing, favouring the co-current drive in the ITER case.
- (x) The large difference in coupling between the heating toroidal phasings is explained by the k_z and k_y spectra of the radiated power and the influence of the density gradient. Indeed, each phasing selects a small domain in the k_y , $|k_z|$ wave spectrum which contributes principally to the loading and, for a given plasma profile, the wave evanescence increases when $|k_z|$ and/or $|k_y|$ increase. As a result, the poorest coupling scenario is the $0\pi 0\pi$ toroidal phasing while the $00\pi\pi$ phasing provides the best power capability. In contrast to the JET situation, the single pass absorption with this last phasing will be high in ITER, on account of its higher expected temperature, and should therefore warrant an excellent heating efficiency [11].
- (xi) The coaxial and surface mode contribution to the loading, which leads to power deposition at the plasma edge, remains low (a few per cent) for all useful heating and current drive scenarios. Only for the case of monopole toroidal phasing an important coaxial and surface modes contribution (up to 50%) is observed.
- (xii) The sensitivity of coupling to variations of the edge density profile has been studied and yielded the following results:
- (a) The part of the edge profile with a density lower than the cut-off density pertaining to the considered phasing does not significantly contribute to the coupling. The density of this part can thus, without loss of coupling, be lowered by the presence of external limiters. For a gas puff to increase the coupling it must be capable to provide density higher than the cut-off density close to the antenna. This cut-off density lies between $4 \times 10^{18} \text{ m}^{-3}$ ($0\pi 0\pi$ phasing) and $7 \times 10^{17} \text{ m}^{-3}$ ($00\pi\pi$ phasing).
 - (b) The displacement of the whole plasma profile 2 cm away from the antenna decreases the power capability of $\sim 25\%$ for all useful heating and current drive phasing except the $0\pi 0\pi$ one which is reduced by $\sim 40\%$. The monopole phasing would only be reduced by 12% on account of the strong, but detrimental, coaxial and surface modes contribution to its loading.
 - (c) A steep density gradient near the plasma bulk significantly reduces the coupling by strong wave reflection. With the same distance cut-off density–antenna, the coupling is worse with large density gradient *even if the bulk plasma is at smaller distance from the antenna*. Such an effect is discussed in [23] in relation to the comparison between the present coupling expectation for ITER with profile Sc2 short17 and the observed (and simulated) coupling to L and H mode in JET.
 - (d) The coupling ratio between the different toroidal phasing cases increases with increasing distance separatrix–antenna and increasing density decay length (up to some limiting value).

Appendix A: The ANTITER II code

Appendix A1. Antenna model used in Antiter II

The fast code Antiter II describes the antenna in plane geometry by an array of boxes recessed in the metal wall, each box being excited by a thin radiating strap. Figure 15 shows the layout of one strap box with an ideal Faraday screen at its mouth (i.e. described by a thin layer of anisotropic conductivity: $\sigma = \infty$ in the z -direction and 0 in the y one). Right-handed rectangular axes with the z -axis along the total steady magnetic field B_0 and the x -axis going outwards of the plasma are used. A vacuum layer of thickness a is assumed in front of the box followed by an inhomogeneous plasma layer (from $x = -x_{\text{edge}}$ up to $x = -x_{\text{bulk}}$) and by a semi-infinite homogeneous bulk plasma (for $x \leq -x_{\text{bulk}}$). The Faraday screen is assumed aligned with B_0 . Therefore only $\text{TE}_{z\perp}$ waves, transverse electric with respect to the z -direction, are excited in the outside medium. These waves have all field components, except E_z which is 0. The metallic boundary condition ($E_y = 0$) is imposed on the wall outside the box apertures. On the box apertures the Fourier series expansion of the tangential fields components inside the box is matched to the $\exp(-i\omega t + ik_z z + ik_y y)$ Fourier integral expansion in the outside medium (see method in [24]).

Please note that in the presence of poloidal magnetic field B_{p0} , the strap position must not be considered with respect to a coordinate system linked to the toroidal and poloidal directions but with respect to axes rotated over α for having their z -axis aligned with B_0 . The mid-strap position is that of the design but the straps are considered perpendicular to B_0 . If the straps are instead perpendicular to the toroidal direction, only the $\text{TE}_{z\perp}$ component of the exciting field will couple to the magnetosonic wave: this introduces a decrease in $(1 - \cos \alpha)\%$ (i.e. of 3.4% for $\alpha = 15^\circ$) of the effective field excitation.

Appendix A2. Description of the fields in the strap box

The $\text{TE}_{z\perp}$ field in the box corresponds to waveguide modes excited far below cut-off because t and w_y are $\ll \lambda_0$ (λ_0 is the vacuum wavelength) by constant surface current distribution J_y at $x = r$. We consider the usual case $v \cong w_y$. J_y is expanded in Fourier series in domain $|z| < t$ and $|y| < w_y$:

$$\begin{aligned} J_y &= \sum J_n \sin \{n\pi(z+t)/(2t)\} [U(y+w_y) - U(y-w_y)] \\ &= \sum J_n X_{n,0}; \quad n = 1, 3, 5, \dots \end{aligned} \quad (\text{A1})$$

with $J_n = [I/(2w_z)][4/(n\pi)] \sin(n\pi/2) \sin(n\pi w_z/(2t))$ and U is the unit step function. This expansion allows us to fulfil the boundary condition $E_y = 0$ on the box sides $z = \pm t$. We express the other boundary conditions (i) in $x = d+r$: $E_y = 0$; (ii) in $x = r$: $\text{curl}_s(H) = J_y$ and continuity of E_y . The tangential field components in $x = 0$ are given by the following expressions:

$$E_y = \sum_n (D_n h_n - J_n l_n) X_{n,0} = \sum_n E_{yn,0} X_{n,0}; \quad (\text{A2})$$

$\omega B_z = \sum_n (D_n f_n - J_n g_n) X_{n,0} = \sum_n \omega B_{zn,0} X_{n,0}$

with $f_n = (1 + \delta\rho)e^{p_n r}$, $g_n = \omega\mu_0(\delta - 1)\rho e^{p_n r}/2$, $h_n = (-ip_n/H_n^2)(\delta\rho - 1)e^{p_n r}$, $l_n = g_n(-ip_n/H_n^2)$, $H_n^2 = k_0^2 - k_{zn}^2$, $p_n^2 = k_{ym}^2 - H_n^2$, $\delta = e^{-2p_n d}$, $\rho = e^{-2p_n r}$ and $k_{zn} = n\pi/(2t)$. The D_n s are the constants to be determined by the continuity of E_y and B_z across the box aperture in $x = 0$.

Appendix A3. Limit of the fields in space $x < 0$ at $x = 0$

The tangential fields are expressed by their Fourier transform $\mathcal{F}\{E_y(x = 0, y, z)\} = E_y(k_y, k_z)$, $\mathcal{F}\{B_z(x = 0, y, z)\} = B_z(k_y, k_z)$ (where $E_y(x = 0, y, z)$ is zero outside the box aperture). Their ratio at $x = 0$ expressed by the normalized surface impedance $\xi_0 = E_y(k_y, k_z)/(\omega B_z(k_y, k_z))$ is obtained as described in section A4 for a non-uniform plasma. The plasma can be replaced by a dielectric [25].

Appendix A4. Plasma description and normalized surface impedance computation

The antenna is loaded by the coupling to the fast magnetosonic wave. Single-pass absorption is assumed in the homogeneous plasma bulk (i.e. no reflection at $x = -\infty$) and numerical integration is performed in the edge plasma profile. The differential equations used to describe the fast magnetosonic wave in the inhomogeneous plasma are [26]

$$\frac{d/dx}{\left\{ \begin{array}{c} i\omega B_z \\ E_y \end{array} \right\}} = \left| \begin{array}{cc} -\mu k_y & -k_\perp^2 \\ 1 - k_y^2/u & \mu k_y \end{array} \right| \left\{ \begin{array}{c} i\omega B_z \\ E_y \end{array} \right\} \quad (\text{A3})$$

with $k_\perp^2 = k_0^2 \varepsilon_1 - k_z^2 - \mu k_0^2 \varepsilon_2$, $\mu = k_0^2 \varepsilon_2 / (k_0^2 \varepsilon_1 - k_z^2)$ and $u = k_0^2 \varepsilon_1 - k_z^2$ where ε_1 and ε_2 are the cold plasma dielectric tensor terms and k_0 the vacuum propagation constant. In the ICRF domain, for single species cold plasma, we have $\varepsilon_1 = 1 - \omega_{pi}^2 / (\omega^2 - \omega_{ci}^2)$ and $\varepsilon_2 = -\omega_{pi}^2 / (\omega^2 - \omega_{ci}^2)(\omega/\omega_{ci})$. The fast magnetosonic wave is also a TE_z wave and all field components can be derived from B_z . We have indeed $k_\perp^2 E_y = -i(d/dx + \mu k_y) \omega B_z$, $k_\perp^2 E_x = -(k_y + \mu d/dx) \omega B_z$, $i\omega B_y = k_z E_x$, $i\omega B_x = -k_z E_y$ and the differential equation for B_z can be obtained from $i\omega B_z = d/dx(E_y) - ik_y E_x$.

The integration is started from the edge of the uniform bulk plasma with an initial condition the value of its normalized surface impedance in the absence of reflection in the bulk plasma $\xi_{\text{bulk}}(k_z, k_y) = \{E_y/(\omega B_z)\}_{\text{bulk plasma edge}} = -i(\mu k_y - i\rho)/k_\perp^2$ where $\rho = (k_\perp^2 - k_z^2)^{1/2}$, the values of μ , k_\perp^2 and ρ being computed for the bulk plasma parameters. $-\rho$ is the perpendicular propagation constant in the uniform bulk plasma (only waves travelling towards $x < 0$). For sufficiently large plasma density $\xi_{\text{bulk}} \approx V_A/\omega$ ($V_A = c\omega_{ci}/\omega_{pi}$, $\omega^2 \gg k_z^2 V_A^2$, $\omega^2 \gg k_y^2 V_A^2$).

The integration allows us to compute the surface impedance ξ_1 at the plasma edge and from ξ_1 to derive the surface impedance in $x = 0$ by the relation $\xi_0 = (-ip/H^2)(i\xi_1 H^2 ch(pa) + psh(pa))/(i\xi_1 H^2 sh(pa) + pch(pa))$ with $H^2 = k_0^2 - k_z^2$, $p^2 = k_y^2 - H^2$ and a being the distance plasma edge–antenna box aperture [17]. The boundary condition at $x = 0_-$ (in the external medium) for the Fourier transform of the exciting field by the boxes is imposed by this $\xi_0(k_z, k_y)$ value.

Appendix A5. Determination of the constants D_n 's. We express the continuity of the tangential fields across $x = 0$

$$\begin{aligned} \omega B_z(x = 0, y, z) &= (1/(2\pi)^2) \iint (E_y(k_y, k_z)/\xi_0) e^{ik_z z + ik_y y} dk_z dk_y \\ &= \Sigma_n (D_n f_n - J_n g_n) X_{n,0} \end{aligned} \quad (\text{A4})$$

where $E_y(k_y, k_z) = \iint \Sigma_n (D_n h_n - J_n l_n) X_{n,0} e^{-ik_z z - ik_y y} dy dz$. As we have

$$\begin{aligned} &\iint X_{n,0} e^{-ik_z z - ik_y y} dy dz \\ &= [n\pi t \cos(k_z t)/(n\pi/2)^2 - (k_z t)^2] (2 \sin(k_y w_y)/k_y) \\ &= \phi_{n,0} \end{aligned} \quad (\text{A5})$$

the continuity of $\omega B_z(x = 0)$ is given by

$$\begin{aligned} &(1/(2\pi)^2) \iint \Sigma_n (D_n h_n - J_n l_n) \phi_{n,0} e^{ik_z z + ik_y y} dk_z dk_y \\ &= \Sigma_n (D_n f_n - J_n g_n) X_{n,0}. \end{aligned} \quad (\text{A6})$$

We multiply the above expression by $X_{j,0}$ and we integrate it in the y, z space over the box aperture. As the functions $X_{n,0}$ are orthogonal we obtain the infinite set of equations

$$\Sigma_n E_{yn,0} \omega \mu_0 Y_{n,0,j,0} = \omega B_{zj,0} \quad \text{with}$$

$$Y_{n,0,j,0} = \{1/(4\pi^2 2w_y t)\} \iint (\phi_{n,0} \phi_{j,0}/\xi_0) dk_z dk_y \quad (\text{A7})$$

If we truncate this set of equations at $n_{\max} = j_{\max}$ we obtain the following relations (for $j = 1, 3, 5, \dots, j_{\max}$) to determine the D_n s from D_1 up to $D_{n_{\max}}$

$$\Sigma_n \{D_n h_n Y_{n,0,j,0}\} - D_j f_j = +\Sigma_n \{J_n l_n Y_{n,0,j,0}\} - J_j g_j. \quad (\text{A8})$$

Therefore, the electric field at the box aperture is given by

$$E_y(x = 0, y, z) = \Sigma_{n=1 \rightarrow n_{\max}} (D_n h_n - J_n l_n) X_{n,0} \quad (\text{A9})$$

and its Fourier transform is

$$\begin{aligned} \mathcal{F}\{E_y(x = 0, y, z)\} &= E_y(k_y, k_z) \\ &= \sigma_{n=1 \rightarrow n_{\max}} (D_n h_n - J_n l_n) \phi_{n,0}. \end{aligned} \quad (\text{A10})$$

Using $n_{\max} = j_{\max} = 5$, a good surface current description on the strap is obtained.

Appendix A6. Electric field of the complete array and total active radiated power

For the ITER array of eight triplets of strap boxes the Fourier transform of the exciting electric field at $x = 0$ of the space $x < 0$ is obtained from the relation:

$$E_{y,\text{array}} = E_y(k_y, k_z) \Sigma_{i=1 \rightarrow 24} e^{(i\Delta\Phi_i + 12k_z S_{z,i} + 12k_y S_{y,i})}, \quad (\text{A11})$$

where $E_y(k_y, k_z)$ is given by equation (A10) and the $\Delta\Phi_i$ are the relative phase of the currents flowing in each triplet. The same current amplitude is assumed in all straps and $S_{z,i}$ and $S_{y,i}$ are the half distances between the triplets in the z - and y -directions with respect to a reference position. In this expression the effect of the mutual coupling between the boxes on $E_y(k_y, k_z)$, i.e. on the single box aperture field $E_y(y, z)$, is neglected.

Appendix A7. Computation of the radiated power. The total active radiated power is obtained from Poynting's vector flux through the surface $x = 0$ (outside medium side)

$$\begin{aligned} 2P_{\text{rad}} &= \text{Re}\{(1/(2\pi)^2) \iint E_y H_z^* dk_z dk_y\} \\ &= \{1/(4\pi^2 \omega \mu_0)\} \text{Re} \left\{ \iint |E_{y,\text{array}}|^2 / \xi_0^* dk_z dk_y \right\}. \end{aligned} \quad (\text{A12})$$

ANTITER II also readily provides the k_y and k_z power spectra. Starting from equation (A12), the mean distributed radiation resistance, for short straps ($2w_y \ll \lambda_0$) as appropriate for ITER, is given by

$$\begin{aligned} \langle R_A \rangle &= \text{Re}(2P_{\text{rad}})/\{|I|^2 24(2w_y)\} \\ &= \int R_{SAy}(k_y) dk_y = \int R_{SAz}(k_z) dk_z, \end{aligned} \quad (\text{A13})$$

where $R_{SAy}(k_y)$ and $R_{SAz}(k_z)$ are, respectively, the k_y and k_z radiation resistance spectrum.

Appendix A8. Computation of the reactive power and the mutual coupling of the straps of the array

The complex Poynting's theorem gives the link between the power supplied by the source in a space domain, the power flux crossing its surface and the rate of change in mean magnetic and electric energy stored within the volume:

$$\begin{aligned} -1/2 \int (E \times H^*) dS \\ = 1/2 \int (E \cdot J^*) dV + i\omega/2 \int [\mu(H \cdot H^*) \\ - \varepsilon(E \cdot E^*)] dV. \end{aligned} \quad (\text{A14})$$

(i) *Case of one single box.* In this case $P_{\text{source}} = 1/2 \int (E \cdot J^*) dV \equiv 1/2 \int (E_y J_y^*) dS_{\text{strap}}$ gives the active and reactive power supplied by the imposed surface current distribution J_y . S_{strap} is the strap surface at $x = r$. The ratio $\{2P_{\text{source}}\}/\{I^2(2w_y)\} = Z_a(1, 1) = R_a(1, 1) + iX_a(1, 1)$ expresses the strap resistance and reactance normalized with respect to its length $2w_y$. The resistance can also be obtained from Poynting's power flux through any surface in vacuum in front of the strap ($r > x > -a$). The reactance is likewise given by the sum of the Poynting vector fluxes through the surfaces $x = r + \varepsilon$ and $x = r - \varepsilon$ with $\varepsilon \rightarrow 0$. The flux through the box opening in $x = 0$ gives only a part of the reactive power as the part corresponding to the difference of magnetic and electric energy inside the box is missing. For our $TE_{z,z}$ excitation the magnetic energy is predominant when $\lambda_0 \gg t$. The electric energy contribution is k_0^2/k_{zn}^2 smaller than the magnetic one for the mode n . The field in the box is then quasi-magnetostatic. When $r \rightarrow 0$ the reactive flux through the $x = 0$ surface contributes to roughly half the total reactive power, the remaining half being in the magnetic energy of the box volume.

(ii) *Case of an array of boxes.* Each diagonal term of the Z matrix is computed as in the single box case. The mutual terms are obtained by the computation of P_{rad} for a number of

different strap phasing combination with the same strap current amplitude $|I|$ giving a number of independent equations equal to the number of $Z_a(i, j)$ terms. As an example, the mutual coupling terms between two straps $Z_a(i, j)$ can be obtained from P_{array} for the corresponding pair of straps excited by the same current magnitude $|I|$ but with phase differences equal to 0 and $\pi/2$. If we note the corresponding P_{rad} by P_0 and $P_{\pi/2}$, respectively, we have the following relations to compute $Z_a(i, j)$ and $Z_a(j, i)$:

$$\begin{aligned} P_0/|I|^2 &= Z_a(i, i) + \{Z_a(i, j) + Z_a(j, i)\}, \\ P_{\pi/2}/|I|^2 &= Z_a(i, i) - \{Z_a(i, j) + Z_a(j, i)\}. \end{aligned} \quad (\text{A15})$$

Exact expressions are obtained for the real part of Z_a . The contribution of the mutual energy term in the box $(1/2) \int \mu(H_i \cdot H_j^*) dV_{\text{BOX}}$ is neglected for the computation of the reactance of the mutual impedance terms $Z_a(i, j)$ and $Z_a(j, i)$.

Euratom © 2010.

References

- [1] Dumortier P. et al 2003 *Proc. 15th Conf. RF Power in Plasmas* (Moran, WY, 2003) AIP Conf. Proc. (Melville, New York 2003) vol 694, ed C. Forest, p 94
<http://proceedings.aip.org/proceedings>
- [2] Jacquinot J. et al 2007 *Proc. 17th Conf. RF Power in Plasmas* (Clearwater, FL, 2007) AIP Conf. Proc. (Melville, NY, 2007) vol 933, ed P. Ryan and D. Rasmussen, p 13
<http://proceedings.aip.org/proceedings>
- [3] Nightingale M. et al 2008 *Proc. 22nd Int Conf. on Fusion Energy 2008* (Geneva, Switzerland, 2008) (Vienna: IAEA) CD ROM file IT/P7-6 and <http://www-naeweb.iaea.org/napc/physics/FEC/FEC2008/html/index.htm>
- [4] Dumortier P. et al 2009 *Fusion Eng. Des.* **84** 707
- [5] Dumortier P. et al 2009 ITER ICRF antenna optimization and broad-banding validation by use of a reduced-scale mock-up *Proc. 18th Conf. RF Power in Plasmas* (Gent, Belgium, 2009), AIP conf. Proc. (Melville, NY, 2009) ed V. Bobkov and J.M. Noterdaeme vol 1187 p 277
- [6] Messiaen A. et al 2009 *Nucl. Fusion* **49** 055004
- [7] Swain D. et al 2009 Status of ITER ICH matching system design *Proc. 18th Conf. RF Power in Plasmas* (Gent, Belgium, 2009), AIP conf. Proc. (Melville, NY, 2009) ed V. Bobkov and J.M. Noterdaeme vol 1187 p 293
- [8] Lancellotti V. et al 2006 *Nucl. Fusion* **46** S476
- [9] Milanesio D. and Maggiore R 2010 ITER ICRF antenna analysis and optimization using the TOPICA code *Nucl. Fusion* **50** 025007
- [10] Messiaen A. et al 2009 Performances of ITER ICRF antenna plug as expected from TOPICA matrices *Proc. 18th Conf. RF Power in Plasmas* (Gent, Belgium, 2009), AIP Conf. Proc. ed V. Bobkov and J.M. Noterdaeme vol 1187 p 269
- [11] Weynants R. 2009 ICRF review: from ERASMUS to ITER *Proc. 18th Conf. RF Power in Plasmas* (Gent, Belgium, 2009), AIP Conf. Proc. (Melville, NY, 2009) ed V. Bobkov and J.M. Noterdaeme vol 1187 p 3
- [12] Lamalle P. et al 2009 Status of the ITER IC H&CD system *Proc. 18th Conf. RF Power in Plasmas* (Gent, Belgium, 2009), AIP conf. Proc. (Melville, NY, 2009) ed V. Bobkov and J.M. Noterdaeme vol 1187 p 265
- [13] CST Microwave Studio, User Manual (Version 2009) (September 2008) (CST AG, Darmstadt, Germany, www.cst.com)

- [14] Loarte A. 2008 private communication
- [15] Loarte A. *et al* 2008 Proc. 22nd Int Conf. on Fusion Energy 2008 (*Geneva, Switzerland, 2008*) (Vienna: IAEA) CD ROM file IT/P6-13 and <http://www-naweb.iaea.org/napc/physics/FEC/FEC2008/html/index.htm>
- [16] Dumortier P. *et al* 2007 Contract FU07-CT 2007-00003 (EFDA/07-1559) *Final Report, LPP-ERM/KMS Laboratory Report No 132*
- [17] Messiaen A. *et al* 1986 *Proc. 13th Conf. on Controlled Fusion and Plasma Heating (Schliersee, Germany, 1986)* vol 10C(ECA) part II (Belgium: European Physical Society) p 125
- [18] Messiaen A. *et al* 1982 *Proc. 3th Int. Symp. on Heating in Toroidal Plasmas (Grenoble, France, 1982)* vol 1 (Belgium: Commission of European Communities) EUR 7979 EN, p 243
- [19] Messiaen A. *et al* 1984 *Proc. 4th Int. Symp. on Heating in Toroidal Plasmas (Roma, Italy, 1984)* vol 1 (Belgium: Commission of European Communities) EUR 9341 EN, p 315
- [20] Swain D. 2009 private communication
- [21] Swain D. 2009 ICDRM-08 (ITER, Cadarache 21 January 2009), <https://user.iter.org/?uid=2M44ET>
- [22] Weynants R.R. *et al* 1980 *2nd Int. Symp. on Heating in Toroidal Plasmas (Como, Italy, 1980)* vol 1 (Belgium: Commission of European Communities) EUR 7424 EN, p 487
- [23] Nightingale M. *et al* 2009 Overview on experiments on ITER-like antenna on JET and ICRF antenna design for ITER *Proc 18th Conf. RF Power in Plasmas (Gent, Belgium, 2009)*, AIP conf. Proc. (*Melville, NY, 2009*) ed V. Bobkov and J.M. Noterdaeme vol 1187 p 213
- [24] Messiaen A. and Weynants R. 1984 *Plasma Phys. Control. Fusion* **26** 525
- [25] Lamalle P. *et al* 2006 *Nucl. Fusion* **46** 432
- [26] Koch R. *et al* 1986 *Comput. Phys. Commun.* **40** 1